

1 **WRN Inhibition Leads to its Chromatin-Associated Degradation Via the PIAS4-RNF4-p97/VCP Axis**

2 Fernando Rodríguez Pérez, Dean Natwick, Lauren Schiff, David McSwiggen, Melina Huey, Alec Heckert,
3 Mandy Loo, Rafael Miranda, Huntly Morrison, Jose Ortega, Renee Butler, Kylie Cheng, John Filbin,
4 Zhengjian Zhang, Eric Gonzalez, Rand Miller, Yangzhong Tang, Jaclyn Ho, Daniel Anderson, Charlene
5 Bashore, Steve Basham

6 **Abstract**

7 Synthetic lethality, the concept in which the co-occurrence of two genetic events leads to cell death while
8 either single event alone does not, is an attractive strategy for targeted cancer therapies. A recent
9 example of synthetic lethality as a therapeutic paradigm is the observation that cancer cells with high
10 levels of microsatellite instability (MSI-H) are dependent on the Werner (WRN) RecQ helicase for survival.
11 However, the mechanisms that regulate WRN spatiotemporal dynamics are not fully understood. In this
12 study, we used our single molecule tracking (SMT) platform in combination with a recently disclosed WRN
13 inhibitor to gain insights into WRN's dynamic localization within the nuclei of live cancer cells. We observe
14 that WRN inhibition results in the helicase becoming trapped on chromatin, requiring p97/VCP for
15 extraction and shuttling to the proteasome for degradation. Interestingly, this sequence of events
16 resulting in WRN degradation appears to be MSI-H dependent. Using a phenotypic screen, we identify the
17 PIAS4-RNF4 axis as the pathway responsible for WRN degradation and show that co-inhibition of WRN
18 and SUMOylation has an additive toxic effect in MSI-H cells. Taken together, our work elucidates a novel
19 regulatory mechanism for WRN. Gaining a deeper understanding into this regulatory pathway for WRN
20 can aid in the identification of new high value targets for targeted cancer therapies.

21 **Main**

22 Werner Syndrome is a rare genetic condition caused by mutations in the *WRN* gene. It is marked by
23 accelerated aging and a predisposition to a variety of cancers (Opresco et al., 2003). The *WRN* gene

24 encodes a RecQ helicase that plays a critical role in genomic integrity and is unique amongst RecQ
25 helicases as it possesses an exonuclease domain in addition to its helicase domain (Croteau et al., 2014).
26 WRN typically resides in the nucleoli of cells but undergoes DNA damage-induced translocation to the
27 nucleoplasm to perform its repair functions, resolving a diverse array of DNA substrates including D-loops,
28 replication forks bubble structures, Holliday junctions and other secondary structures. (Constantinou et
29 al., 2000; von Kobbe and Bohr 2002; Bendtsen et al., 2014). Additionally, WRN is required for telomere
30 maintenance, a necessary process for maintaining stem cell cellular homeostasis (Shen and Loeb 2001).

31 Synthetic lethality has emerged as an appealing approach to target cancer cells while minimizing
32 collateral damage to otherwise healthy cells and tissue (O'Neil et al., 2017). Synthetic lethality occurs
33 when there is simultaneous disturbance of two essential biological events leading to cell death, which
34 would not occur in the presence of one genetic disruption alone. To highlight the importance of WRN in
35 DNA repair, WRN has been identified as a synthetic lethal target in microsatellite instability high (MSI-H)
36 tumor types that are deficient in mismatch repair (MMR) pathways (Chan et al., 2019; Kategaya et al.,
37 2019; Lou et al., 2019; Picco et al., 2021). Microsatellites are short tandem repeats of repetitive
38 nucleotides that reside throughout the genome. Microsatellite stable (MSS) cells have two DNA repair
39 mechanisms - (1) MMR machinery and (2) WRN to ensure genetic integrity. In MSS cells, disruption to
40 either MMR or WRN does not lead to cell death. However, in MSI-high cells, MMR processes are
41 compromised so the combination of inhibiting WRN leads to cell death due to this synthetic lethal
42 relationship (Chan et al., 2019; Lieb et al., 2019; Picco et al., 2021). This WRN synthetic modality can be
43 exploited for therapeutic value and has recently entered the clinic for the treatment of MSI-H cancers
44 (NCT05838768 2018; NCT06004245 2023). A deeper understanding of DNA replication and repair
45 regulatory mechanisms may provide insights that can be exploited for therapeutic-based purposes. Here,
46 we present the identification of a new WRN degradation mechanism revealed by single molecule tracking
47 (SMT). Upon WRN inhibition, WRN becomes trapped on chromatin and is SUMOylated by PIAS4.

48 SUMOylated WRN is recognized by the ubiquitin E3 ligase RNF4, which then ubiquitinates WRN leading to
49 p97/VCP-mediated chromatin extraction and ultimately proteasomal dependent degradation, providing
50 new avenues for therapeutic targeting.

51 To investigate the consequence of WRN inhibition in WRN dynamics, we utilized a recently
52 published clinical WRN inhibitor HRO761 (WRNi, Fig. 1a) (NCT05838768 2018) (Bordas et al., 2022). We
53 first established a panel of MSI-H and MSS cells and tested for WRN sensitivity by depleting WRN using
54 siRNAs (Extended Data Fig. 1a-d). Testing this compound in cells showed a >100-fold induction of DNA
55 damage response in MSI-H cells compared to MSS cells, resulting in apoptosis and cell death (Fig. 1b-d,
56 Extended Data Fig. 1g). Additionally, cellular toxicity was only observed in MSI-H, but not MSS cells, further
57 highlighting the specificity of WRNi (Fig. 1e, Extended Data Fig. 1h). To profile the specificity of this
58 compound *in vitro*, we purified WRN protein and its related homologue, BLM (Extended Data Fig. 1e-f).
59 Using this recombinant system, we observed a 1000-fold difference in ATPase and helicase inhibition with
60 WRN vs BLM (Fig. 1f-g, Extended Data Fig. 1i-j). Further highlighting the accumulation of DNA damage by
61 WRNi, we observed an increase in nuclear size, indicative of DNA damage accumulation and potential cell
62 senescence prior to apoptosis (Extended Data Fig. 2a-b) (Dedov et al., 2003; Rello-Varona et al., 2006;
63 Kang et al., 2010). To enable imaging of proteins at the single molecule level we used CRISPR to generate
64 endogenous HaloTagTM WRN fusion protein (WRN^{Halo}) in MSS (U2OS) and MSI-H (HCT-116) cells
65 (McSwiggen et al., 2023). Prior to our imaging studies, we validated the successful tagging of WRN in these
66 cells by depleting the HaloTagTM WRN signal using a HaloTagTM PROTAC (Extended Data Fig. 2c-d).
67 Furthermore, comparison between WT and HaloTagTM-WRN HCT-116 cells showed no discernable
68 differences between the two upon WRN inhibition (Extended Data Fig. 2e).

69 WRN undergoes a sub-compartmental translocation in response to DNA damage using standard
70 immunofluorescence (Marciniak et al., 1998; von Kobbe and Bohr 2002). As previously reported, we
71 observed robust translocation of WRN from the nucleolus to the nucleoplasm upon induction of DNA

72 damage (Fig. 2a) (Kamath-Loeb et al., 2017; Veith et al., 2019; Zhu et al., 2021). We employed SMT to
73 understand the link between WRN enzymatic activity mobility in cells using WRNi. Our fully automated
74 SMT platform enables the measurement of thousands of experimental conditions and millions of cells per
75 day (McSwiggen 2023). Recently we introduced substantial improvements to the platform, utilizing a light-
76 sheet-based illumination strategy that improves both the throughput and quality of the SMT platform
77 (Driouchi et al., submitted). Upon WRNi treatment, we observed a significant and dose-dependent
78 decrease in average WRN mobility in the HCT-116 background (Fig. 2b-d, Extended Data Fig. 2f). Strikingly,
79 no changes in protein diffusion coefficient were observed in U2OS, suggesting that the microsatellite state
80 of the cell influenced the effect of WRNi on WRN dynamics (Fig. 2c, Extended Data Fig. 2g). Due to the
81 virtue of SMT being a single molecule assay, we next sought to extract a more granular view of dynamic
82 states of WRN in cells. To this end, we plotted the proportion of WRN proteins moving at a particular
83 diffusion rate to generate a “state array” that provides a glimpse of the various states in which WRN is
84 found, ranging from an immobile chromatin-bound state to a freely diffusing state (McSwiggen et al.,
85 2023). We observed a decrease in the fastest-diffusing states and more than a 2-fold increase in the
86 chromatin bound fraction of WRN in HCT-116 cells upon WRNi treatment (Fig. 2e-g). In contrast, we did
87 not observe these changes in microsatellite stable U2OS cells or with treatment of general DNA damaging
88 compounds (Fig. 2c and Extended Data Fig. 2g). The observed decrease in WRN diffusion coefficient was
89 subsequently followed by a decrease in SMT spot density, suggesting possible degradation of the WRN
90 protein (Fig. 2h).

91 We confirmed this observation by performing a WRNi time-course which resulted in a reduction
92 of WRN protein levels in HCT-116 cells but not U2OS cells (Fig. 3a-b, Extended Data Fig. 3c). WRN
93 degradation does not result from general DNA damage, but instead is specific to WRNi in a dose-
94 dependent and proteasomal dependent way, as co-treatment of HCT-116 with the proteasome inhibitor
95 carfilzomib rescues this effect (Extended Data Fig. 3a-b). Using cycloheximide, we determined that WRN

96 inhibition reduced the half-life of WRN protein by over an order of magnitude, from 16.6h to 1.5h (Fig.
97 3b, and Extended Data Fig. 3d). The increased proportion of chromatin-bound (“bound”) WRN molecules,
98 and the concomitant decrease in the freely diffusing (“fast”) population, shown in the state array data,
99 suggests that inhibition of WRN by WRNi leads to its trapping on DNA (Fig. 2e-g). This mode of action has
100 been widely studied with PARP1 and its inhibitors (Helleday 2011; Lord and Ashworth 2017).

101 To investigate whether a similar mechanism of action was occurring upon WRN inhibition, we
102 treated WRN^{Halo} cells with WRNi followed by permeabilization with a mild detergent to liberate soluble
103 contents of the cells followed by fixation for immunolocalization studies (Illuzzi et al., 2022). These
104 solubilization experiments revealed that treatment with WRNi led to the accumulation of WRN bound to
105 chromatin based on the retention of WRN signal detected in the nucleus after treatment with detergent
106 (Fig. 3d, 3k). Strikingly, we also observed increased colocalization of ubiquitin and WRN upon treatment
107 with WRNi, further fortifying the link between WRN inhibition and the ubiquitin-proteasome pathway
108 (Fig. 3d-f). This link was also validated by using tandem ubiquitin binding entities (TUBEs), which revealed
109 a clear enrichment of higher molecular weight WRN species after WRNi treatment (Fig. 3g). Taken
110 together, these data indicate that WRN is ubiquitylated upon its inhibition. Consistent with the lack of
111 γH2A.X induction observed in U2OS cells upon WRN inhibition, WRNi treatment in this MSS background
112 did not result in WRN trapping or degradation, suggesting that microsatellite instability plays a role in the
113 regulation of WRN upon its inhibition (Fig. 3c, 3h, 3l and Extended Data Fig. 3e). Replication machinery
114 has the potential to become stalled on DNA due to blockade by other bound proteins or DNA lesions
115 (Edenberg et al., 2014; Liao et al., 2018; Le et al., 2023). To mitigate trapping, cells take advantage of
116 ubiquitin-mediated proteasomal degradation in which these stalled proteins are marked for degradation
117 by classical proteasome pathways after ubiquitin deposition (Vaz et al., 2013; Franz et al., 2016; Challa et
118 al., 2021). p97/VCP has been implicated in the extraction of ubiquitylated membrane-bound, and
119 chromatin-bound proteins. Therefore, we next investigated if the p97/VCP-proteasome axis was

120 responsible for degradation of WRN (Rape et al., 2001; Jarosch et al., 2002; Wojcik et al., 2004; Meyer et
121 al., 2012). Indeed, upon co-treatment with p97/VCP or proteasome inhibitors we were able to rescue the
122 WRN degradation phenotype induced by WRNi in HCT-116 cells, suggesting an endogenous ubiquitin-
123 dependent regulatory paradigm for WRN (Fig. 3i, Extended Data Fig. 3f). This finding was further validated
124 using cellular SMT (Extended Data Fig. 3g) (Kim and Crews 2013; Anderson et al., 2015). Having
125 determined that WRN degradation by WRNi treatment is mediated by the p97/VCP-proteasome axis, we
126 next set out to identify the ubiquitin E3 ligase that activates this process. Depletion of E3 ligases, MIB1
127 and MDM2, that have been reported to regulate WRN did not prevent the degradation of WRN protein
128 upon WRN inhibition (Extended Data Fig. 4a) (Liu et al., 2019; Li et al., 2020). Therefore, we set out to
129 perform a ubiquitome-focused phenotypic siRNA screen and identified six potential genes that upon
130 knock-down rescue WRNi-mediated degradation of WRN or regulate WRN protein levels in other ways
131 (Fig. 4a and Extended Data Fig. 4b). Further validation of these siRNA hits identified RNF4 as the ligase
132 responsible for WRN degradation upon WRNi treatment (Fig. 4a-b). Knock-down of RNF4 showed the most
133 significant rescue of the phenotype, with all RNF4 siRNA oligos rescuing WRN protein levels to at least
134 75% of control treated cells (Extended Data Fig. 4c). We speculate that the partial rescues from the other
135 ubiquitin modulators indicate putative genetic interactors, but the lack of a full rescue effect suggests
136 these are not direct modulators, such as UBE2D3, which is a known E2 conjugating enzyme for RNF4 (Fig.
137 4c and Extended Data Fig. 4c) (DiBello et al., 2016; Roman-Trufero and Dillon 2022). We also observed a
138 rescue of the WRN degradation phenotype using SMT by measuring the density of WRN molecules after
139 RNF4 siRNA knock-down (Extended Data Fig. 4d). Depletion of RNF4 abolished the ubiquitylation of WRN
140 after WRNi treatment, further establishing that RNF4 is responsible for WRN degradation (Fig. 4d-f and
141 Extended Data Fig. 4e). Surprisingly, depletion of RNF4 only slightly rescued the change in WRN diffusion
142 coefficient after inhibition by WRNi, suggesting that WRN remains trapped on chromatin in the absence
143 of ubiquitylation (Fig. 4g). Trapped WRN is detrimental for genome integrity, and failure to remove and

144 degrade trapped WRN results in further DNA damage, as evidenced by increased γH2A.X accumulation
145 following knockdown of RNF4 (Ext data fig 4f). Co-treatment with the E1 ubiquitin activating enzyme
146 inhibitor TAK-234 (E1i) and WRNi led to a slight decrease in the diffusion coefficient of WRN, which could
147 suggest that inhibited WRN remains bound to chromatin if it cannot be ubiquitylated (Hyer et al., 2018)
148 (Fig. 4h). State array analysis revealed that the global inhibition of ubiquitylation by E1i alone led to an
149 increase in the slow diffusing fraction of WRN protein (Fig. 4i, j). This indicates that ubiquitylation is indeed
150 required for the regulation of WRN beyond its function to drive protein degradation as has been shown
151 for various cellular processes (Manford et al., 2020; Rodriguez-Perez et al., 2021; Padovani et al., 2022).
152 However, the state array analysis also revealed that co-treatment with E1i and WRNi lead to a slight but
153 significant increase in the chromatin bound fraction of WRN (Fig. 4i, k). Taken together, these data suggest
154 that WRN inhibition in MSI-H cells leads to an increase in chromatin binding, followed by ubiquitylation
155 and subsequent degradation. This ubiquitylation is necessary to remove WRN from chromatin, as
156 exemplified by the increase in WRN bound to chromatin in the presence of an E1 inhibitor. RNF4 is known
157 as a SUMO-targeted ubiquitin ligase (STUBL) and has been reported to regulate trapped chromatin
158 proteins such as PARP1, DNMT1, and TOP1A (Sun et al., 2020; Liu et al., 2021; Krastev et al., 2022). To
159 investigate if SUMOylation is required for the degradation of inhibited WRN, we depleted cells of the
160 SUMO ligase PIAS4. The depletion of PIAS4 provided a modest, yet significant rescue of WRN degradation
161 upon WRNi treatment (Fig. 5a, 5c). We posit that this failure to completely rescue the degradation
162 phenotype is due to redundancies among the different PIAS proteins. To investigate this, we co-treated
163 cells with the SUMO E1 activating enzyme inhibitor ML-792 (SUMOi) and WRNi, leading to a full rescue of
164 the degradation phenotype by various means of detection, including SMT (Fig. 5b-f and Extended Data
165 Fig. 6a-b) (He et al., 2017). Furthermore, upon SUMOylation inhibition, we failed to pull down
166 ubiquitylated WRN even in the presence of WRNi (Fig. 5g), indicating that the SUMO cascade is necessary
167 to initiate ubiquitylation of WRN. This is evident by the appearance of higher molecular weight WRN,

168 which corresponds to ubiquitylated and SUMOylated WRN, as they disappear upon co-treatment with
169 SUMO_i (Fig. 5h). Co-treatment with SUMO_i and WRN_i lead to a further decrease in WRN diffusion
170 coefficient (Fig. 5i). State array analysis indicated that this decrease was due to an increase in the “slow”
171 fraction of WRN, further suggesting that the SUMO/ubiquitin cascade is important for the regulation of
172 inhibited WRN (Fig. 5j). Indeed, inhibition of the SUMO-Ubiquitin-p97/VCP cascade lead to an increase in
173 chromatin-bound WRN following inhibition by WRN_i (Extended Fig. 5a-b). Taken together, these data
174 clearly show that small molecule inhibition of WRN leads to its trapping onto chromatin, leading to its
175 SUMOylation and subsequent ubiquitylation by RNF4 which ultimately results in proteasomal degradation
176 (Fig. 5m). This work has elucidated a novel molecular pathway that regulates WRN activity upon its
177 inhibition. The identification of WRN as a synthetic lethal target in MSI-H cancers has opened new avenues
178 for therapeutic intervention of these malignancies. Clinical medicine has been successful in the selective
179 killing of cancer cells mediated by DNA binding protein inhibition [etoposide citation]. For example, the
180 enzyme, Poly ADP-ribose polymerase (PARP) can induce specific cell toxicity by PARP trapping. PARP
181 carries out its enzymatic function by repairing single-stranded DNA breaks, but inhibition leads to trapping
182 on DNA. As a result, PARP function is attenuated leading to an accumulation of DNA damage, stalled
183 replication forks and cytotoxicity (Shen et al., 2015; Hopkins et al., 2019; Rose et al., 2020). Understanding
184 the mechanistic underpinnings of WRN regulation has implications for treating MSI-H cancers in the clinic.
185 WRN that cannot be released from chromatin after trapping is detrimental and leads to persistent DNA
186 damage, even after removal of WRN inhibition (Fig. 5l and Extended Data Fig. 6c-d). This regulatory
187 cascade has various points in which potential therapeutic interventions are possible, such as co-inhibition
188 of the SUMOylation cascade or depletion of RNF4, which results in synergistic shift in the EC₅₀ of WRN_i
189 (Fig. 5k and Extended Data Fig. 6e-h). Many other areas of potential intervention exist, such as disruption
190 of the translocation of WRN from the nucleolus to the nucleoplasm, or perturbation of the molecular
191 players that recognize chromatin-trapped WRN protein. This work provides deeper insights into the

192 regulation of WRN protein activity upon small molecule inhibition that was gained in part through cutting-
193 edge super resolution microscopy techniques like cellular SMT. Such detailed understanding will likely be
194 critical in defining optimal clinical strategies as first-in-class WRN inhibitors undergo clinical testing.

195 **Acknowledgements**

196 The authors extend their deepest gratitude to all the employees and consultants of Eikon, past and
197 present, especially, Pratir Doshi, Nick Vaquera, Jeff Dove, Tiffany Cheng, Roma Moore, Bruno da Rocha
198 Azevedo, Madhu Mena, Emily Kirkeby, Puneet Kumar, Dave Piotrowski, Melissa Dumble, Geeta Sharma,
199 and Alex Therian. Their tireless work enabled the experiments described here. We thank Roger
200 Perlmutter, Robert Tjian for helpful discussions and critical feedback on the direction of our investigation
201 and on the resulting manuscript. Eikon Therapeutics provided all funding.

202 **Declaration of interests**

203 The authors are employees and/or shareholders of Eikon Therapeutics.

204

205 **Materials and Methods:**

206 ***Tissue Culture***

207 HCT-116 (MSI genotype), U2OS, RKO, SW48, DLD-1 and HT-29 (MSS genotype) cells were used.
208 Cells were cultured in Gibco McCoy's 5A Medium (Thermo, 16600082) containing 10% fetal bovine serum
209 (FBS), 1X GlutaMAX supplement (Thermo, 35050061), 1X MEM Non-Essential Amino Acids solution
210 (Thermo, 11140076) and 50,000 Units/µg of Penicillin/Streptomycin (Thermo, 15140122) at 37°C and 5%
211 CO₂. Cells were seeded on Greiner 384-Well Black Microplate with Optical-Bottom (Greiner, 781906) using
212 a Thermo Multidrop Combi. HCT-116 cells were seeded at 2,500 cells per well and HT-29 cells were seeded
213 at 3,000 cells per well and incubated at 37°C and 5% CO₂ for 24 hours before compound treatment.
214 Compounds were added to the plates using a Beckman Echo 655 acoustic liquid handler. Compound
215 treated plates were incubated for 24 h at 37°C and 5% CO₂.

216 ***Cell Line Engineering***

217 WRN^{Halo} HCT-116 and U2OS were generated by nucleofection of ribonucleoprotein (RNP)
218 complexes (DeWitt et al., 2017) using a guide (5' – AAAGATGAGTGA~~AAAAAA~~AT – 3') targeting the N-
219 terminus of the *WRN* gene locus and a megamer coding for the Halo tag as a donor template (5' –
220 TATTGTATCTGTTTGTGATTCTAGCTCTATAACCTATGCTTGGACCTAGGTGTCAACTACTTAAATAT
221 GTATGTTGGTTTCATTCATATTGACAGTACTACCTCTCAGTTTCTTCAGATATTGTTGTATTACCATGAAG
222 ACATTGTTTTGGACTCTGCAAATACCACATTCAAAGATGGCAGAAATCGGTACTGGCTTCCATTGACCCCCA
223 TTATGTGGAAGTCCTGGCGAGCGCATGCACTACGTCATGTTGGTCCCGCGATGGCACCCCTGTGCTGTTCTG
224 CACGGTAACCCGACCTCCTCCTACGTGTGGCGAACATCATCCCGATGTTGCACCGACCCATCGCTGCATTGCTCC
225 AGACCTGATCGGTATGGCAAATCCGACAAACCAGACCTGGTTATTCTCGACGACCACGTCCGCTTATGGAT
226 GCCTTCATCGAAGCCCTGGGTCTGGAAGAGGTCGTCTGGTCATTCACGACTGGGGCTCGCTGGGTTCCACT
227 GGGCCAAGCGCAATCCAGAGCGCGTAAAGGTATTGCATTATGGAGTTATCCGCCCTATCCGACCTGGGACG
228 AATGGCCAGAATTGCCCGAGACCTCCAGGCCTCCGACCCACCGACGTCGGCCGCAAGCTGATCATCGATCA

229 GAACGTTTTATCGAGGGTACGCTGCCGATGGGTGTCGTCCGCCGCTGACTGAAGTCGAGATGGACCATTACCG
230 CGAGCCGTTCTGAATCCTGTTGACCGCGAGCCACTGTGGCGCTCCAAACGAGCTGCCAATGCCGGTGAGCC
231 AGCGAACATCGTCGCGCTGGTCGAAGAATACTGGACTGGCTGCACCAGTCCCTGTCCGAAGCTGCTGTTCTG
232 GGGCACCCCAGGCCTCTGATCCCACCGGCCGAAGCCGCTGCCCTGCCAAAAGCCTGCCTAACTGCAAGGCTGT
233 GGACATCGGCCCGGGTCTGAATCTGCTGCAAGAAGACAACCCGGACCTGATCGGCAGCGAGATCGCGCGCTGGC
234 TGTCGACGCTCGAGATTCCGGCGAAAACCTGTATTTCAGAGCAGTGAAAAAAAATTGGAAACAAC TGCAACAGC
235 AGCGGAAATGTCCTGAATGGATGAATGTGCAGAATAAAAGATGTGCTGTAGAAGAAAGAAAGGTATGTTGTTCAT
236 TGACTATTCTTTGGGTGAGAAATTAAATTATTTGACTGTGCAAAGAGTCAGTTGTTACTTGAAACTTCAAGT
237 CATTGTTAGGTAGAG – 3'). RNPs were assembled with Alt-R™ S.p. HiFi Cas9 Nuclease V3 (IDT, 1081060)
238 in a 10 µl reaction of 1 µM of Cas9, 120 pmol sgRNA, and 100 pmol ssODN in Cas9 buffer (20 mM HEPES
239 7.5, 150 mM KCl, 10% glycerol, 1 mM TCEP). Reactions were gently mixed for 30s and incubated for 10min
240 at room temperature. RNP complexes and 200k cells resuspended in 20 µl buffer SE (Lonza) were added
241 to a nucleofection strip and the mixture pulsed with program EH-100 (Lonza 4D-Nucleofector). Cells were
242 plated into 96-well plates for recovery with a fresh media change after 1 day. Two days after RNP
243 electroporation, pooled cells then were single-cell seeded into 384-well plates. After single-cell derived
244 clones emerged, they were split into 2 plates, one of which was used to detect positive clones containing
245 the desired HaloTag™ sequence through Sanger sequencing.

246 ***Antibodies and Reagents***

247 Goat anti-Rabbit IgG Alexa Fluor Plus 647 (Thermo, A32733), anti-phospho-Histone H2A.X
248 (Ser139)-clone JBW301 (γH2A.X, Millipore, 05-636-I), anti-WRN clone EPR6392 (abcam, ab124673), Goat
249 anti-Rabbit IgG (H+L)-HRP (Invitrogen, 31460), anti-GAPDH-HRP (CST, 31460), anti-Ubiquitin, clone P4D1
250 (for WB; CST, 3936), anti-Ubiquitin, clone FK2 (For IF; Millipore sigma, 04-263), anti-SUMO-2/3, clone 18H8
251 (CST, 4971S), anti-phospho-CHK1 (Ser345; CST, 2341), phospho-Chk2 (Thr68; clone C13C1; CST, 2661),

252 cleaved PARP1 (Asp214; clone D64E10; CST, 5625), anti-RNF4 (R&D Systems, AF7964), anti-MDM2 (R&D
253 Systems, D1V2Z), anti-MIB1 (CST, 4400).

254 JF549 (Promega, GA1110), etoposide (CST, 2200), 5-FU (5-fluorouracil; Selleckchem, S1209),
255 doxorubicin (CST, 5927), HaloPROTAC3 (Promega, GA3110), HaloPROTAC-E (MedChem Express, HY-
256 145752), MLN-4924 (CST, 85923), carfilzomib (CST, 15022), TAK-243 (MedChem Express, HY-100487), ML-
257 792 (MedChem Express, HY-108702).

258 ***Immunofluorescence and DNA Damage Quantification***

259 Cell culture medium was removed using the Blue Cat Bio Blue®Washer. Paraformaldehyde
260 solution (8% PFA (Electron Microscopy Sciences, 15710-S), 1X phosphate buffered solution (PBS) (Teknova
261 P0191)) was added to the cells via Thermo Multidrop® Combi and treated for 7 min at room temperature
262 to fixate the cells. The paraformaldehyde solution was removed with the Blue Cat Bio BlueWasher. Triton
263 solution (0.1% TritonX-100 (Sigma, T8787), 1X PBS) was added to the cells via Thermo Multidrop Combi
264 and treated for 15 min at room temperature to permeabilize the cells. The triton solution was removed
265 with the Blue Cat Bio BlueWasher. Serum solution (10% Goat Serum (Gibco, 16210), 1X PBS) was added
266 to the cells via Thermo Multidrop Combi and treated for 15 min at room temperature to block the cells.
267 The serum solution was removed with the Blue Cat Bio BlueWasher. Primary antibody solution (1:1000
268 primary antibody, 10% Goat Serum, 1X PBS) was added to the cells via a Thermo Multidrop Combi and
269 treated for 3 hours at room temperature with shaking. The primary antibody solution was removed with
270 the Blue Cat Bio BlueWasher. Secondary antibody solution (secondary antibody (1:1000), Hoechst 33342
271 (AnaSpec, AS-83210) (1:3000), 10% Goat Serum, 1X PBS) was added to the cells via Thermo Multidrop
272 Combi and treated for 30 min at room temperature, covered from light, with shaking. Cells were washed
273 with PBS 3 times using the Blue Cat Bio BlueWasher with a final dispense of PBS. Sealed plates were
274 imaged using an ImageXpress Micro slit confocal microscope (Molecular Devices) using a 40x water
275 immersion objective, and 6 fields of view per well. Exposure parameters were optimized to prevent pixel

276 saturation for each channel. Images were analyzed using MetaXpress Custom Module Editor, by using a
277 Hoechst mask to identify nuclei, then measuring the integrated AlexaFluor 648 intensity across all nuclei
278 in the field of view (FOV) and then averaged. Percent γH2A.X signal was calculated by using the following
279 equation: $\%S = (T - C_{pos})/(C_{pos} - C_{neg}) * 100$, where $\%S$ is percent γH2A.X signal and T is the measured
280 γH2A.X fluorescence of the wells treated with test compound. The effective compound concentration
281 leading to a 50% induction of γH2A.X signal (EC_{50}), and the resulting cell γH2A.X signal measured at the
282 highest tested compound tested (C_{max}) was carried out by fitting a 4-parameter non-linear regression using
283 GraphPad Prism. At least three biological replicates were done per compound tested.

284 ***Western Blotting***

285 Samples were lysed in 1x NuPAGE LDS sample buffer (Invitrogen, NP0008), sonicated, and heated
286 at 75 °C for 10 min. Samples were normalized to protein concentration and volume using a Pierce 660
287 reagent kit (Invitrogen, 22660). SDS-Page was performed using standard protocols (ref). Western blot
288 transfers were performed using an iBlot2 nitrocellulose membrane system (Invitrogen, IB23001).
289 Membranes were blocked with Pierce™ Protein-Free Blocking Buffer (Thermo Scientific, 37572) for 30 min
290 at room temperature, and subsequently probed with desired antibodies.

291 ***Cell Viability Assay***

292 To seed cells, cells were trypsinized and resuspended in complete culture media to the desired
293 concentration (HCT-116: 10,000 cells/mL; RKO: 15,000 cells/mL; SW-48, HT-29, and SW-480: 25,000
294 cells/mL; U2OS: 7,000 cells/mL). Cell suspensions were seeded in 50 µL of complete culture media and
295 plated onto 384-well white clear-bottom plates (ThermoFisher Cat# 164610) using a Multidrop™ Combi
296 liquid dispenser in the slowest setting in triplicate. After 24 h, cells were treated with compounds in a 10-
297 pt, 3.16 step serial dilution using an Echo acoustic liquid dispenser (Beckman). DMSO was backfilled to a
298 final concentration of 0.1%. 10 µM etoposide (C_{pos}) and DMSO (C_{neg}) were used as reference compounds.
299 96 h post compound addition, plates were evacuated to decant all media. To measure viability, cellular

300 ATP concentrations were measured by adding 20 μ L of 1x CellTiterGlo 2.0 (CTG) solution (1 part PBS, 1
301 part CellTiterGlo2.0 stock solution; Promega Cat# G9241) using a MultidropTM Combi liquid dispenser
302 and measuring the luminescence on a SpectraMax iD3 (Molecular Devices).
303 Percent viability was calculated by the following equation: $\%V = (T - C_{pos})/(C_{pos} - C_{neg}) * 100$, where $\%V$ is
304 percent viability and T is the measured luminescence of the wells treated with test compound. The
305 effective compound concentration leading to a 50% reduction in viability (EC_{50}), and the resulting cell
306 viability measured at the highest tested compound tested (c_{max}) was carried out by fitting a 4-parameter
307 non-linear regression using GraphPad Prism. At least three biological replicates were done per compound
308 tested.

309 ***Tandem Ubiquitin Binding Entities (TUBE) Pull Down***

310 HCT-116 cells were grown as described above. 10^6 cells were seeded on 10 cm tissue culture
311 dishes (ThermoFisher, 150464), and allowed to attach for 48h. Cells were subsequently treated with
312 compounds for 8 h ($[ML-792] = 1 \mu\text{M}$, $[Carfilzomib] = 10 \text{ nM}$, $[TAK-243] = 10 \text{ nM}$, $[WRNi] = 10 \mu\text{M}$),
313 harvested by trypsinization, centrifuged (300 $\times g$), and flash frozen in liquid nitrogen. Cell pellets were
314 lysed in 500 μL of TUBE lysis buffer (150 mM NaCl, 2 mM MgCl₂, 25 mM HEPES pH 7.0, 0.03% SDS, 1 M
315 urea, 10 μM PR-619, 1x protease inhibitor cocktail) for 10 min on ice, with frequent mixing. While cell lysis
316 was occurring, 100 μL of slurry/reaction of TUBE magnetic beads (UM501M, LifeSensors) were washed in
317 1x PBS three times, and once with TUBE lysis buffer. After cell lysis, lysates were cleared (20,000 $\times g$, 10
318 min), inputs were taken, and lysates were subsequently added to TUBE magnetic beads. Lysate-TUBE bead
319 mixtures were incubated at 4 °C on a nutator for 2 h. Samples were subsequently washed five times with
320 TUBE wash buffer (150 mM NaCl, 2 mM MgCl₂, 25 mM HEPES pH 7.0, 0.5% Triton X-100, 1 M urea), and
321 resuspended in 1X LDS buffer to prepare for downstream Western blot analysis.

322 ***HaloTagTM Protein labeling***

323 Cells were seeded in black 384-well plates using a combidrop multidrop dispenser and seeded for
324 at least 24 h in complete growth media at either 45K cells/mL or 100K cells/mL, depending on the
325 experiment. To label HaloTagged proteins, JF549 (Promega, GA1110) was added to cells using an Echo
326 acoustic liquid dispenser to a final concentration of 25 pM. Cells were incubated at 37 °C for 2 h, and
327 subsequently washed 5 times in PBS, with the final wash leaving the wells empty. After washing, cells
328 were either fixed in 4% paraformaldehyde (Electron Microscopy Sciences, 15710), or growth media was
329 replenished to perform subsequent compound treatments.

330 ***WRN Imaging Degradation Assays***

331 Cell lines and growth conditions are identical to the above conditions. To seed cells for the assay,
332 cells were trypsinized and resuspended in complete culture media to the desired concentration (WRN^{Halo}
333 HCT-116: 50,000 cells, WRN^{Halo} U2OS: 30,000 cells/mL). Cell suspensions were seeded in 50 µL of complete
334 culture media and onto 384-well black clear-bottom optical plastic plates (Greiner Bio-One Cat# 781097)
335 using a MultidropTM Combi liquid dispenser in the slowest setting in triplicate. After 24 h, cells were labeled
336 with Halo dye as described above and subsequently treated with compounds in a 10-pt, 3.16 step serial
337 dilution using an Echo acoustic liquid dispenser and incubated at 37 °C in a humidified 5% CO₂ incubator.
338 10 µM Halo-PROTAC3 (C_{pos}; Promega, GA3110) and DMSO (C_{neg}) were used as reference compounds. 24 h
339 after compound treatments, cells were fixed in 4% paraformaldehyde for 10 min, washed three times with
340 PBS, then blocked and permeabilized in PBS containing 10% goat serum and 0.1% triton X-100 containing
341 the DNA counterstain Hoechst for 30 min. Plates were washed 3 times in PBS, and sealed with thermal foil
342 seals.

343 Sealed plates were imaged using an ImageXpress Micro slit confocal microscope (Molecular
344 Devices) using a 40x water immersion objective, and 6 fields of views per well. Exposure parameters were
345 optimized to prevent pixel saturation for each channel. Images were analyzed using MetaXpress Custom

346 Module Editor, by using a Hoechst mask to identify nuclei, then measuring the average Halo dye intensity
347 across all nuclei in the FOV, averaged, and then background subtracted.

348 Percent WRN^{Halo} signal was calculated by using the following equation: %S = (T - C_{pos})/(C_{pos} - C_{neg}) *
349 100, where %S is percent WRN^{Halo} signal and T is the measured WRN^{Halo} fluorescence of the wells treated
350 with test compound. The effective compound concentration leading to a 50% induction of WRN^{Halo} signal
351 (EC₅₀), and the resulting cell WRN^{Halo} signal measured at the highest tested compound tested (C_{max}) was
352 carried out by fitting a 4-parameter non-linear regression using GraphPad Prism. At least three biological
353 replicates were done per compound tested.

354 ***Phenotypic Screening and Imaging***

355 An arrayed human ON-TARGETplus ubiquitome siRNA SMARTpool library (Horizon Discovery,
356 106205-E2-01) was resuspended to a final concentration of 20 uM in 1x siRNA Buffer (Horizon Discovery,
357 B-002000-UB-100). siRNA oligos were transferred onto black 384 µClear plates using an Echo acoustic
358 dispenser to yield a final oligo concentration of 20 nM. 5 µL of opti-MEM (Gibco, 31985062) was added to
359 resuspend transferred oligos. RNA oligo:lipid complexes were formed by adding 0.3 µL of Lipofectamine
360 RNAiMAX (Invitrogen, 13778075) in 5 µL of opti-MEM. Complexes were incubated for 5 min before
361 dispensing 50 µL of HCT-116 cells (100K cells/mL) and incubating in growth conditions described above.
362 After 24 h, growth media was exchanged, and labeled with HaloTagTM dye as described above. WRNi, or
363 DMSO, was added at a final concentration of 10 µM, treated for 24 h, and subsequently fixed with 4%
364 PFA. Cells were permeabilized with 0.1% triton-x 100 for 20 min to remove non-specific dye staining and
365 imaged as described above.

366 ***siRNA Depletions***

367 Cells were processed as described for quantifying WRN levels after siRNA knock-down. For
368 Western blot analysis, HCT-116 (90K cells/well) or U2OS (60K cells/well) cells were seeded in 6-well TC
369 treated plates (Corning, 3516). siRNA depletions were performed following the recommended protocol

370 for Lipofectamine RNAiMax. Samples were harvested in 1x LDS sample buffer and prepared for Western
371 blot analysis as described.

372 ***WRN In-Situ Trapping Assay***

373 WRN^{Halo} Cells (HCT-116 or U2OS) were seeded in black 384-well plates using a combidrop
374 multidrop dispenser and seeded for 48 h in complete media at 100K cells/mL (HCT-116) or 30 K cells/mL
375 (U2OS). Cells were labeled with HaloTag™ Dye and subsequently treated with desired compounds as
376 described above for 8 h ([ML-792] = 1 μ M, [Carfilzomib] = 10 nM, [TAK-243] = 10 nM, [WRNi] = 10 μ M).
377 Following compound treatments, samples were decanted to remove all media and treated with ice cold
378 CSK buffer (25 mM PIPES pH 7.0, 300 mM NaCl, 2 mM MgCl₂, 0.3 % TritonX-100, 200 mM sucrose) for 2
379 min, on ice. Without removing buffer in wells, cells were fixed in 4% PFA supplemented with Hoechst for
380 15 min and washed with 1x PBS 5 times using an AquaMax Plate washer (Molecular Devices). Samples
381 were then imaged as described above. Quantifications were done by measuring the total intensity of the
382 Halo dye signal and using the Hoechst channel as a nuclear mask.

383 ***Protein Purification***

384 Human WRN residues 480–1251 were cloned into pFastBac vector containing an 8xHis N-terminal
385 tag and expressed in Sf9 insect cells. Harvested cells were resuspended in lysis buffer (50 mM HEPES, pH
386 7.5, 500 mM NaCl, 25 mM imidazole, 1mM TCEP, 5 U/mL benzonase (Millipore Sigma), EDTA-free
387 cOmplete protease inhibitor cocktail tablet (Roche)) and lysed by addition of Insect PopCulture reagent
388 (Millipore Sigma). Lysate was loaded on to a HiTrap TALON Crude column (Cytiva) and protein was eluted
389 using 500mM Imidazole. Fractions containing WRN protein were collected, pooled, then diluted to in
390 buffer to drop the NaCl concentration to ~100mM. The pooled and diluted sample was then loaded onto
391 a heparin column (Cytiva) and eluted using a step-wise gradient from 200mM to 1000mM NaCl. Fractions
392 containing purified WRN protein were pooled, and buffer exchanged into 50mM HEPES, 150mM NaCl,
393 10% glycerol, 1mM TCEP using a HiPrep desalting column (Cytiva).

394 Human BLM residues 636-1298 were cloned into pFastBac vector containing an 8xHis N-terminal
395 tag and expressed in Sf9 insect cells. Harvested cells were resuspended in lysis buffer (50 mM HEPES, pH
396 8, 200 mM NaCl, 0.5mM TCEP, 5 U/mL benzonase (Millipore Sigma), EDTA-free cOmplete protease
397 inhibitor cocktail tablet (Roche)) and lysed by addition of Insect PopCulture reagent (Millipore Sigma).
398 Lysate was loaded onto a Ni-NTA column (Thermo Fisher) and protein was eluted using 300mM Imidazole.
399 Fractions containing BLM protein were collected, pooled, and diluted in buffer to drop the NaCl
400 concentration to ~50mM. The pooled and diluted sample was then loaded on a HiTrap Heparin column
401 (Cytiva) and eluted with a linear gradient from 50mM to 1M NaCl. The pure fractions were pooled and
402 concentrated and purified by size exclusion chromatography using S200 Increase (Cytiva) in 50mM HEPES
403 pH 8, 200mM NaCl, 5% glycerol, 0.5mM TCEP.

404 ***Helicase Unwinding and ATPase Assay***

405 The helicase unwinding and ATPase were carried out in a multiplexed fashion based on previously
406 published BLM assay (Chen et al., 2021) . Single-stranded DNA was purchased from IDT:
407 A: 5'-Cy3-GAACGAACACATGGGTACGTTTTTTTTTTTTTTTTTTTTTTTTTTTTTTTT
408 B: 5'-TTTTTTTTTTTTTTTTTTTTTTTTTTTTTCGTACCCGATGTGTTCGTTC-IowaBlackFQ-3'
409 B-dark: 5'-CGTACCCGATGTGTTCGTTCY-3'
410 Strands A and B were annealed in TE + 50mM NaCl in a slowly-cooling thermocycler.
411 First, compounds in DMSO were dispensed to a 384-well white ProxiPlate (Perkin Elmer) using an Echo
412 acoustic liquid handler. WRN or BLM Protein was diluted into assay buffer and 2.5 μ L was dispensed into
413 each well. Protein and compound then incubated at room temperature for 15 min. Following pre-
414 incubation, 2.5 μ L of DNA and ATP in assay buffer was dispensed into each well to initiate the reaction and
415 incubated for 20 min at room temperature. At the 20 minute time point, Cy3 fluorescence was read on an
416 Envision plate reader to measure unwinding activity. ATP hydrolysis was then measured using ADP-Glo kit
417 (Promega) by adding 5uL ADP-Glo reagent for 40 minutes followed by 10uL Kinase Detection Reagent for

418 1hour. Luminescence was measured using Envision plate reader. Data was normalized to DMSO (100%
419 activity). The final reaction conditions are: 1mM ATP, 15nM dsDNA substrate, 1.5uM B-dark in reaction
420 buffer composed of 50mM Tris-HCl pH 8.0, 50mM NaCl, 2mM MgCl₂, 0.01% Tween-20, 2.5μg/mL poly(dI-
421 dC), 1mM DTT, 1% DMSO, and 12.5nM WRN or 2.5nM BLM.

422 ***Cellular SMT Sample preparation***

423 For SMT experiments, WRN Halo-tagged HCT-116 cells were seeded in FluoroBrite DMEM
424 (Thermo Fisher, cat. no. 1896701) supplemented with 10% FBS (Corning), 1% Penicillin/Streptomycin
425 (Gibco, 1510-122), and 1% GlutaMAX (Gibco, 35050-061) on plasma-coated 384-well glass-bottom plates
426 (Cellvis, P384-1.5H-N) at 1.5x10⁴ cells per well. WRN Halo-tagged U2OS cells were seeded in GlutaMAX-
427 supplemented DMEM (Gibco, 10566-016) with 10% FBS and 1% Penicillin/Streptomycin at 6x10³ cells per
428 well. Prior to treatment and imaging, HCT-116 cells were incubated at 37 °C and 5% CO₂ for ~48 hours to
429 allow for cell adherence to the plates, while U2OS cells were incubated under the same conditions for 24
430 hours. For all SMT experiments, cells were treated with 10-40 pM of JF549-HTL (synthesized in-house) and
431 200 nM Hoechst 33342 (Thermo Fisher, cat. No. 62249) for 1 hour in complete medium at 37 °C and 5%
432 CO₂. Cells were then washed three times in PBS and twice in FluoroBrite DMEM supplemented with 2%
433 FBS, 1% Penicillin/Streptomycin, and 1% GlutaMAX. All compounds were prepared on Echo Qualified 384-
434 Well Low Dead Volume Source Microplates (Labcyte, cat. No. LP-0200) in DMSO and administered onto
435 cells at a final 1:500 dilution in cell culture medium. Unless otherwise specified, cells were incubated with
436 compounds for 4 hours at 37 °C prior to image acquisition. When possible, well replicate conditions were
437 randomized across each plate. For all experiments, control conditions included vehicle (DMSO) treatment
438 and wells lacking JF549-HTL to assess possible effects from detection of non-dye signal.

439 ***Cellular SMT Image Acquisition***

440 Unless otherwise stated, all image acquisition for cSMT was performed on a customized Nikon
441 Eclipse Ti2-E inverted fluorescence microscope with a motorized stage. The microscope system was

442 outfitted with a stage top environmental chamber with temperature and CO₂ control (OKO labs), Nikon
443 objective water dispenser, an Oblique Line Scanning (OLS) illumination module (Driouchi et al., submitted)
444 with laser launch containing 405 nm, 560 nm, and 642 nm lasers, three-band emission filter set (ET
445 445/58m, FF01-585/40-25, FF01-676/37-25, Chroma), motorized filter wheel (Lambda 10-B; Sutter
446 Instruments), and a high-speed sCMOS camera equipped with light-sheet mode capability (ORCA-Fusion
447 BT, Hamamatsu). Images were acquired with a 60X 1.27 NA water immersion objective (CFI SR Plan Apo IR
448 60XC WI, Nikon, Japan). The environmental chamber was maintained at 37° C, 95% humidity, and 5% CO₂.
449 For each field of view, 150 SMT frames were collected at a frame rate of 100 Hz with a 407-microsecond
450 stroboscopic laser pulse, and 1 frame in the Hoechst channel was subsequently collected for downstream
451 registration of trajectories to nuclei. Each frame captured an FOV that was 1728 x 2304 pixels (187.14 x
452 249.52 microns) in size. Automated microscope control and image acquisition was performed using
453 customized scripts in MicroManager.

454 For all experiments, conditions were tested by acquiring JF549 movies and Hoechst images at 4
455 FOVs per well, a minimum of 2 well replicates per plate, and a minimum of 2 plate replicates. Unless
456 otherwise stated, reported averages for each condition are the mean value of all FOVs collected. For time
457 course experiments, reported averages at each time point are the mean value of all FOVs collected across
458 6 consecutive wells per plate replicate.

459 ***Cellular SMT Image Processing***

460 Image acquisition yielded one JF549 movie and one Hoechst movie per FOV. The JF549 movie was
461 used to track the motion of individual JF549 molecules, while the Hoechst movie was used for nuclear
462 segmentation.

463 For tracking, we used a custom pipeline that operates in three sequential steps. First, dye molecules are
464 detected using a generalized log likelihood ratio detector (Serge et al., 2008). The position of each
465 detected emitter is then estimated using a Levenberg-Marquardt fitting routine (Levenberg 1944;

466 Marquardt 1963; Laurence and Chromy 2010) with an integrated 2D Gaussian spot model (Smith et al.,
467 2010) starting from an initial guess afforded by the radial symmetry method (Parthasarathy 2012).
468 Detected emitters were then linked into trajectories using a custom algorithm. Briefly, this method first
469 estimates the marginal probabilities of each potential link between particles using the graphical softmax
470 operator (Cuturi 2013; Mena et al., 2018) applied to a Brownian motion model, then attempts to find the
471 set of trajectories with maximum marginal log probability using a modification of Sbalzerini's hill-climbing
472 algorithm (Sbalzarini and Koumoutsakos 2005). Identical tracking settings were used for all movies in this
473 manuscript.

474 For nuclear segmentation, all frames of the Hoechst movie were averaged to generate a mean
475 projection. This mean projection was then segmented with a UNET-based convolutional neural network
476 trained on human-labeled nuclei (Ronneberger et al., 2015). Each spot was then assigned to at most one
477 nucleus using its subpixel coordinates. To recover dynamical information from trajectories, we used state
478 arrays (Heckert et al., 2022), a Bayesian inference approach, with the “RBME” likelihood function and a
479 grid of 100 diffusion coefficients from 0.01 to 100.0 $\mu\text{m}^2/\text{sec}$ and 31 localization error magnitudes from
480 0.02 μm to 0.08 μm (1D RMSD). After inference, localization error was marginalized out to yield a one-
481 dimensional distribution over the diffusion coefficient for each FOV.

482 ***Synthesis of HRO761***

483 The WRN inhibitor HRO761 was synthesized following an established synthesis route for Compound 42,
484 as described in WO2022/249060. (Bordas et al., 2022).

485 **References**

486 Anderson, D. J., R. Le Moigne, S. Djakovic, B. Kumar, J. Rice, S. Wong, J. Wang, B. Yao, E. Valle, S. Kiss von
487 Soly, A. Madriaga, F. Soriano, M. K. Menon, Z. Y. Wu, M. Kampmann, Y. Chen, J. S. Weissman, B. T. Aftab,
488 F. M. Yakes, L. Shawver, H. J. Zhou, D. Wustrow and M. Rolfe (2015). "Targeting the AAA ATPase p97 as an
489 Approach to Treat Cancer through Disruption of Protein Homeostasis." *Cancer Cell* **28**(5): 653-665.

490 Bendtsen, K. M., M. B. Jensen, A. May, L. J. Rasmussen, A. Trusina, V. A. Bohr and M. H. Jensen (2014).
491 "Dynamics of the DNA repair proteins WRN and BLM in the nucleoplasm and nucleoli." *Eur Biophys J*
492 **43**(10-11): 509-516.

493 Bordas, V., J. Brun, A. Decker, M. Furegati, G. Gogniat, W. Gong, J. Hamon, J. H.-H. Hinrichs, P. Holzer, F.
494 Limam, H. Moebitz, S. Nocito, S. Plattner, N. Schmiedeberg, J. Schoepfer, J. Soto, R. Strang, S. Yao, H. Yu,
495 F. Zecri and S. Zhang. WO 2022/249060 A1 (2022). "Triazolo-pyrimidine analogues for treating diseases
496 connected to the inhibitor of werner syndrome recq helicase (wrn)" Novartis AG.

497 Challa, K., C. D. Schmid, S. Kitagawa, A. Cheblal, V. Iesmantavicius, A. Seeber, A. Amitai, J. Seebacher, M.
498 H. Hauer, K. Shimada and S. M. Gasser (2021). "Damage-induced chromatome dynamics link Ubiquitin
499 ligase and proteasome recruitment to histone loss and efficient DNA repair." *Mol Cell* **81**(4): 811-829 e816.

500 Chan, E. M., T. Shibue, J. M. McFarland, B. Gaeta, M. Ghandi, N. Dumont, A. Gonzalez, J. S. McPartlan, T.
501 Li, Y. Zhang, J. Bin Liu, J. B. Lazaro, P. Gu, C. G. Piett, A. Apffel, S. O. Ali, R. Deasy, P. Keskula, R. W. S. Ng, E.
502 A. Roberts, E. Reznichenko, L. Leung, M. Alimova, M. Schenone, M. Islam, Y. E. Maruvka, Y. Liu, J. Roper,
503 S. Raghavan, M. Giannakis, Y. Y. Tseng, Z. D. Nagel, A. D'Andrea, D. E. Root, J. S. Boehm, G. Getz, S. Chang,
504 T. R. Golub, A. Tsherniak, F. Vazquez and A. J. Bass (2019). "WRN helicase is a synthetic lethal target in
505 microsatellite unstable cancers." *Nature* **568**(7753): 551-556.

506 Chen, X., Y. I. Ali, C. E. Fisher, R. Arribas-Bosacoma, M. B. Rajasekaran, G. Williams, S. Walker, J. R. Booth,
507 J. J. Hudson, S. M. Roe, L. H. Pearl, S. E. Ward, F. M. Pearl and A. W. Oliver (2021). "Uncovering an allosteric
508 mode of action for a selective inhibitor of human Bloom syndrome protein." *eLife* **10**.

509 Constantinou, A., M. Tarsounas, J. K. Karow, R. M. Brosh, V. A. Bohr, I. D. Hickson and S. C. West (2000).
510 "Werner's syndrome protein (WRN) migrates Holliday junctions and co-localizes with RPA upon
511 replication arrest." *EMBO Rep* **1**(1): 80-84.

512 Croteau, D. L., V. Popuri, P. L. Opresko and V. A. Bohr (2014). "Human RecQ helicases in DNA repair,
513 recombination, and replication." *Annu Rev Biochem* **83**: 519-552.

514 Cuturi, M. (2013). "Sinkhorn Distances: Lightspeed Computation of Optimal Transportation Distances."
515 *Advances in Neural Information Processing Systems* **26**: 2292-2300.

516 Dedov, V. N., I. V. Dedova and G. A. Nicholson (2003). "Inhibition of topoisomerase II overrides the G2/M
517 check points of the cell cycle in EBV-lymphocytes." *Apoptosis* **8**(4): 399-406.

518 DiBello, A., A. B. Datta, X. Zhang and C. Wolberger (2016). "Role of E2-RING Interactions in Governing
519 RNF4-Mediated Substrate Ubiquitination." *Journal of Molecular Biology* **428**(23): 4639-4650.

520 Edenberg, E. R., M. Downey and D. Toczyński (2014). "Polymerase stalling during replication, transcription
521 and translation." *Curr Biol* **24**(10): R445-452.

522 Franz, A., P. A. Pirson, D. Pilger, S. Halder, D. Achuthankutty, H. Kashkar, K. Ramadan and T. Hoppe (2016).
523 "Erratum: Chromatin-associated degradation is defined by UBXN-3/FAF1 to safeguard DNA replication
524 fork progression." *Nature Communications* **7**(1): 11593.

525 He, X., J. Riceberg, T. Soucy, E. Koenig, J. Minissale, M. Gallery, H. Bernard, X. Yang, H. Liao, C. Rabino, P.
526 Shah, K. Xega, Z.-h. Yan, M. Sintchak, J. Bradley, H. Xu, M. Duffey, D. England, H. Mizutani, Z. Hu, J. Guo,
527 R. Chau, L. R. Dick, J. E. Brownell, J. Newcomb, S. Langston, E. S. Lightcap, N. Bence and S. M. Pulukuri
528 (2017). "Probing the roles of SUMOylation in cancer cell biology by using a selective SAE inhibitor." *Nature
529 Chemical Biology* **13**(11): 1164-1171.

530 Heckert, A., L. Dahal, R. Tjian and X. Darzacq (2022). "Recovering mixtures of fast-diffusing states from
531 short single-particle trajectories." *eLife* **11**: e70169.

532 Helleday, T. (2011). "The underlying mechanism for the PARP and BRCA synthetic lethality: clearing up the
533 misunderstandings." *Mol Oncol* **5**(4): 387-393.

534 Hopkins, T. A., W. B. Ainsworth, P. A. Ellis, C. K. Donawho, E. L. DiGiammarino, S. C. Panchal, V. C. Abraham,
535 M. A. Algire, Y. Shi, A. M. Olson, E. F. Johnson, J. L. Wilsbacher and D. Maag (2019). "PARP1 Trapping by
536 PARP Inhibitors Drives Cytotoxicity in Both Cancer Cells and Healthy Bone Marrow." *Molecular Cancer
537 Research* **17**(2): 409-419.

538 Hyer, M. L., M. A. Milhollen, J. Ciavarri, P. Fleming, T. Traore, D. Sappal, J. Huck, J. Shi, J. Gavin, J. Brownell,
539 Y. Yang, B. Stringer, R. Griffin, F. Buzzese, T. Soucy, J. Duffy, C. Rabino, J. Riceberg, K. Hoar, A. Lublinsky,
540 S. Menon, M. Sintchak, N. Bump, S. M. Pulukuri, S. Langston, S. Tirrell, M. Kuranda, P. Veiby, J. Newcomb,
541 P. Li, J. T. Wu, J. Powe, L. R. Dick, P. Greenspan, K. Galvin, M. Manfredi, C. Claiborne, B. S. Amidon and N.
542 F. Bence (2018). "A small-molecule inhibitor of the ubiquitin activating enzyme for cancer treatment."
543 *Nature Medicine* **24**(2): 186-193.

544 Illuzzi, G., A. D. Staniszewska, S. J. Gill, A. Pike, L. McWilliams, S. E. Critchlow, A. Cronin, S. Fawell, G.
545 Hawthorne, K. Jamal, J. Johannes, E. Leonard, R. Macdonald, G. Maglennon, J. Nikkila, M. J. O'Connor, A.
546 Smith, H. Southgate, J. Wilson, J. Yates, S. Cosulich and E. Leo (2022). "Preclinical Characterization of
547 AZD5305, A Next-Generation, Highly Selective PARP1 Inhibitor and Trapper." *Clin Cancer Res* **28**(21): 4724-
548 4736.

549 Jarosch, E., C. Taxis, C. Volkwein, J. Bordallo, D. Finley, D. H. Wolf and T. Sommer (2002). "Protein
550 dislocation from the ER requires polyubiquitination and the AAA-ATPase Cdc48." *Nat Cell Biol* **4**(2): 134-
551 139.

552 Kamath-Loeb, A. S., D. G. Zavala-van Rankin, J. Flores-Morales, M. J. Emond, J. M. Sidorova, A. Carnevale,
553 M. D. Cardenas-Cortes, T. H. Norwood, R. J. Monnat, L. A. Loeb and G. E. Mercado-Celis (2017).
554 "Homozygosity for the WRN Helicase-Inactivating Variant, R834C, does not confer a Werner syndrome
555 clinical phenotype." *Sci Rep* **7**: 44081.

556 Kategaya, L., S. K. Perumal, J. H. Hager and L. D. Belmont (2019). "Werner Syndrome Helicase Is Required
557 for the Survival of Cancer Cells with Microsatellite Instability." *iScience* **13**: 488-497.

558 Kim, K. B. and C. M. Crews (2013). "From epoxomicin to carfilzomib: chemistry, biology, and medical
559 outcomes." *Nat Prod Rep* **30**(5): 600-604.

560 Krastev, D. B., S. Li, Y. Sun, A. J. Wicks, G. Hoslett, D. Weekes, L. M. Badder, E. G. Knight, R. Marlow, M. C.
561 Pardo, L. Yu, T. T. Talele, J. Bartek, J. S. Choudhary, Y. Pommier, S. J. Pettitt, A. N. J. Tutt, K. Ramadan and
562 C. J. Lord (2022). "The ubiquitin-dependent ATPase p97 removes cytotoxic trapped PARP1 from
563 chromatin." *Nat Cell Biol* **24**(1): 62-73.

564 Laurence, T. A. and B. A. Chromy (2010). "Efficient maximum likelihood estimator fitting of histograms."
565 *Nature Methods* **7**(5): 338-339.

566 Le, T. T., M. Wu, J. H. Lee, N. Bhatt, J. T. Inman, J. M. Berger and M. D. Wang (2023). "Etoposide promotes
567 DNA loop trapping and barrier formation by topoisomerase II." *Nature Chemical Biology* **19**(5): 641-650.

568 Levenberg, K. (1944). "A method for the solution of certain non-linear problems in least squares." *Quart.
569 Appl. Math.* **2**: 164-168.

570 Li, M., B. Liu, J. Yi, Y. Yang, J. Wang, W.-G. Zhu and J. Luo (2020). "MIB1-mediated degradation of WRN
571 promotes cellular senescence in response to camptothecin treatment." *The FASEB Journal* **34**(9): 11488-
572 11497.

573 Liao, H., F. Ji, T. Helleday and S. Ying (2018). "Mechanisms for stalled replication fork stabilization: new
574 targets for synthetic lethality strategies in cancer treatments." *EMBO reports* **19**(9): e46263.

575 Lieb, S., S. Blaha-Ostermann, E. Kamper, J. Rippka, C. Schwarz, K. Ehrenhöfer-Wölfer, A. Schlattl, A.
576 Wernitznig, J. J. Lipp, K. Nagasaka, P. van der Lelij, G. Bader, M. Koi, A. Goel, R. A. Neumüller, J.-M. Peters,
577 N. Kraut, M. A. Pearson, M. Petronczki and S. Wöhrle (2019). "Werner syndrome helicase is a selective
578 vulnerability of microsatellite instability-high tumor cells." *eLife* **8**: e43333.

579 Liu, B., J. Yi, X. Yang, L. Liu, X. Lou, Z. Zhang, H. Qi, Z. Wang, J. Zou, W.-G. Zhu, W. Gu and J. Luo (2019).
580 "MDM2-mediated degradation of WRN promotes cellular senescence in a p53-independent manner."
581 *Oncogene* **38**(14): 2501-2515.

582 Liu, J. C. Y., U. Kühbacher, N. B. Larsen, N. Borgermann, D. H. Garvanska, I. A. Hendriks, L. Ackermann, P.
583 Haahr, I. Gallina, C. Guérillon, E. Branigan, R. T. Hay, Y. Azuma, M. L. Nielsen, J. P. Duxin and N. Mailand
584 (2021). "Mechanism and function of DNA replication-independent DNA-protein crosslink repair via the
585 SUMO-RNF4 pathway." *The EMBO Journal* **40**(18): e107413.

586 Lord, C. J. and A. Ashworth (2017). "PARP inhibitors: Synthetic lethality in the clinic." *Science* **355**(6330):
587 1152-1158.

588 Lou, K., L. A. Gilbert and K. M. Shokat (2019). "A Bounty of New Challenging Targets in Oncology for
589 Chemical Discovery." *Biochemistry* **58**(31): 3328-3330.

590 Manford, A. G., F. Rodriguez-Perez, K. Y. Shih, Z. Shi, C. A. Berdan, M. Choe, D. V. Titov, D. K. Nomura and
591 M. Rape (2020). "A Cellular Mechanism to Detect and Alleviate Reductive Stress." *Cell* **183**(1): 46-61 e21.

592 Marciniak, R. A., D. B. Lombard, F. B. Johnson and L. Guarente (1998). "Nucleolar localization of the
593 Werner syndrome protein in human cells." *Proc Natl Acad Sci U S A* **95**(12): 6887-6892.

594 Marquardt, D. W. (1963). "An Algorithm for Least-Squares Estimation of Nonlinear Parameters." *Journal*
595 *of the Society for Industrial and Applied Mathematics* **11**(2): 431-441.

596 McSwiggen, D. T., H. Liu, R. Tan, S. A. Puig, L. B. Akella, R. Berman, M. Bretan, H. Chen, X. Darzacq, K. Ford,
597 R. Godbey, E. Gonzalez, A. Hanuka, A. Heckert, J. J. Ho, S. L. Johnson, R. Kelso, A. Klammer, J. Li, K. Lin, B.
598 Margolin, P. McNamara, L. Meyer, S. E. Pierce, A. Sule, Y. Tang, D. J. Anderson and H. P. Beck (2023). "High-
599 throughput single molecule tracking identifies drug interactions and cellular mechanisms." *bioRxiv*:
600 2023.2001.2005.522916.

601 Mena, G., D. Belanger, S. Linderman and J. Snoek (2018). "Learning Latent Permutations with Gumbel-
602 Sinkhorn Networks." *International Conference on Learning Representations*.

603 Meyer, H., M. Bug and S. Bremer (2012). "Emerging functions of the VCP/p97 AAA-ATPase in the ubiquitin
604 system." *Nat Cell Biol* **14**(2): 117-123.

605 NCT05838768 (2018). "Study of HRO761 Alone or in Combination in Cancer Patients With Specific DNA
606 Alterations Called Microsatellite Instability or Mismatch Repair Deficiency." *Clinicaltrials.gov*.

607 NCT06004245 (2023). "A Study to Evaluate the Safety, Pharmacokinetics, and Anti-Tumor Activity of
608 RO7589831 in Participants With Advanced Solid Tumors." *Clinicaltrials.gov*.

609 O'Neil, N. J., M. L. Bailey and P. Hieter (2017). "Synthetic lethality and cancer." *Nat Rev Genet* **18**(10): 613-
610 623.

611 Opresko, P. L., W. H. Cheng, C. von Kobbe, J. A. Harrigan and V. A. Bohr (2003). "Werner syndrome and
612 the function of the Werner protein; what they can teach us about the molecular aging process." *Carcinogenesis* **24**(5): 791-802.

613 Padovani, C., P. Jevtic and M. Rape (2022). "Quality control of protein complex composition." *Mol Cell*
614 **82**(8): 1439-1450.

615 Parthasarathy, R. (2012). "Rapid, accurate particle tracking by calculation of radial symmetry centers."
616 *Nature Methods* **9**(7): 724-726.

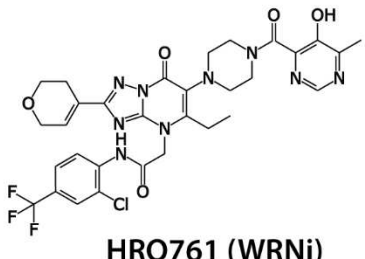
617 Picco, G., C. M. Cattaneo, E. J. van Vliet, G. Crisafulli, G. Rospo, S. Consonni, S. F. Vieira, I. S. Rodriguez, C.
618 Cancelliere, R. Banerjee, L. J. Schipper, D. Oddo, K. K. Dijkstra, J. Cinatl, M. Michaelis, F. Yang, F. Di
619 Nicolantonio, A. Sartore-Bianchi, S. Siena, S. Arena, E. E. Voest, A. Bardelli, M. J. Garnett and U. K. G. Cell
620 Model Network (2021). "Werner Helicase Is a Synthetic-Lethal Vulnerability in Mismatch Repair-Deficient
621 Colorectal Cancer Refractory to Targeted Therapies, Chemotherapy, and Immunotherapy." *Cancer Discov*
622 **11**(8): 1923-1937.

623

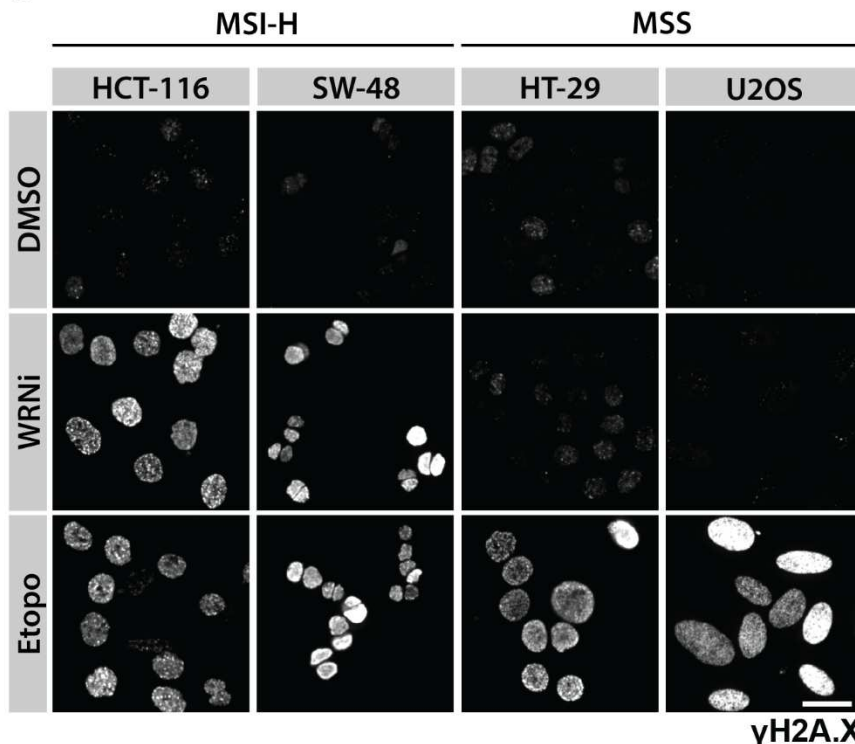
624 Rape, M., T. Hoppe, I. Gorr, M. Kalocay, H. Richly and S. Jentsch (2001). "Mobilization of processed,
625 membrane-tethered SPT23 transcription factor by CDC48(UFD1/NPL4), a ubiquitin-selective chaperone." *Cell* **107**(5): 667-677.
626
627 Rodriguez-Perez, F., A. G. Manford, A. Pogson, A. J. Ingersoll, B. Martinez-Gonzalez and M. Rape (2021).
628 "Ubiquitin-dependent remodeling of the actin cytoskeleton drives cell fusion." *Dev Cell* **56**(5): 588-601
629 e589.
630 Roman-Trufero, M. and N. Dillon (2022). "The UBE2D ubiquitin conjugating enzymes: Potential regulatory
631 hubs in development, disease and evolution." *Frontiers in Cell and Developmental Biology* **10**.
632 Ronneberger, O., P. Fischer and T. Brox (2015). *U-Net: Convolutional Networks for Biomedical Image*
633 *Segmentation*. Medical Image Computing and Computer-Assisted Intervention – MICCAI 2015, Cham,
634 Springer International Publishing.
635 Rose, M., J. T. Burgess, K. O'Byrne, D. J. Richard and E. Bolderson (2020). "PARP Inhibitors: Clinical
636 Relevance, Mechanisms of Action and Tumor Resistance." *Front Cell Dev Biol* **8**: 564601.
637 Sbalzarini, I. F. and P. Koumoutsakos (2005). "Feature point tracking and trajectory analysis for video
638 imaging in cell biology." *Journal of Structural Biology* **151**(2): 182-195.
639 Serge, A., N. Bertaux, H. Rigneault and D. Marguet (2008). "Dynamic multiple-target tracing to probe
640 spatiotemporal cartography of cell membranes." *Nat Methods* **5**(8): 687-694.
641 Shen, J. and L. A. Loeb (2001). "Unwinding the molecular basis of the Werner syndrome." *Mech Ageing*
642 *Dev* **122**(9): 921-944.
643 Shen, Y., M. Aoyagi-Scharber and B. Wang (2015). "Trapping Poly(ADP-Ribose) Polymerase." *Journal of*
644 *Pharmacology and Experimental Therapeutics* **353**(3): 446-457.
645 Smith, C. S., N. Joseph, B. Rieger and K. A. Lidke (2010). "Fast, single-molecule localization that achieves
646 theoretically minimum uncertainty." *Nature Methods* **7**(5): 373-375.
647 Sun, Y., L. M. Miller Jenkins, Y. P. Su, K. C. Nitiss, J. L. Nitiss and Y. Pommier (2020). "A conserved SUMO
648 pathway repairs topoisomerase DNA-protein cross-links by engaging ubiquitin-mediated proteasomal
649 degradation." *Sci Adv* **6**(46).
650 Vaz, B., S. Halder and K. Ramadan (2013). "Role of p97/VCP (Cdc48) in genome stability." *Frontiers in*
651 *Genetics* **4**.
652 Veith, S., A. Schink, M. Engbrecht, M. Mack, L. Rank, P. Rossatti, M. Hakobyan, D. Goly, T. Hefele, M.
653 Frensch, A. Fischbach, A. Bürkle and A. Mangerich (2019). "PARP1 regulates DNA damage-induced
654 nucleolar-nucleoplasmic shuttling of WRN and XRCC1 in a toxicant and protein-specific manner." *Scientific*
655 *Reports* **9**(1): 10075.
656 von Kobbe, C. and V. A. Bohr (2002). "A nucleolar targeting sequence in the Werner syndrome protein
657 resides within residues 949-1092." *J Cell Sci* **115**(Pt 20): 3901-3907.
658 Wojcik, C., M. Yano and G. N. DeMartino (2004). "RNA interference of valosin-containing protein
659 (VCP/p97) reveals multiple cellular roles linked to ubiquitin/proteasome-dependent proteolysis." *J Cell Sci*
660 **117**(Pt 2): 281-292.
661 Zhu, M., W. Wu, Y. Togashi, W. Liang, Y. Miyoshi and T. Ohta (2021). "HERC2 inactivation abrogates
662 nucleolar localization of RecQ helicases BLM and WRN." *Scientific Reports* **11**(1): 360.

Figure 1

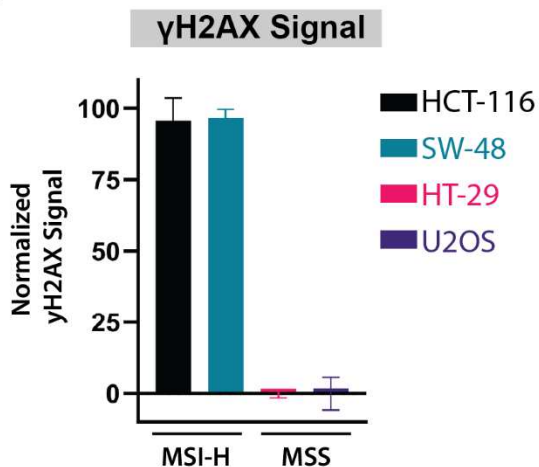
a



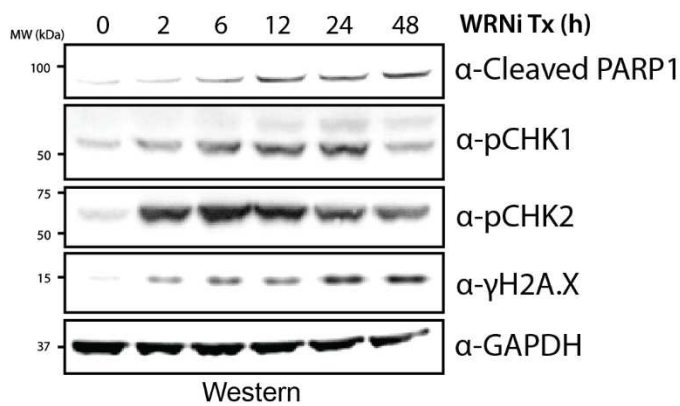
b



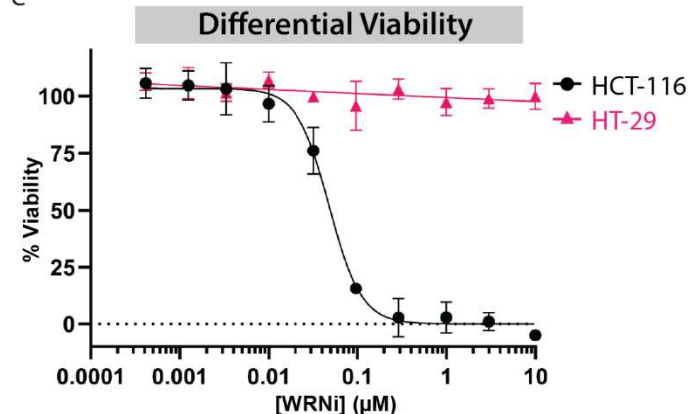
c



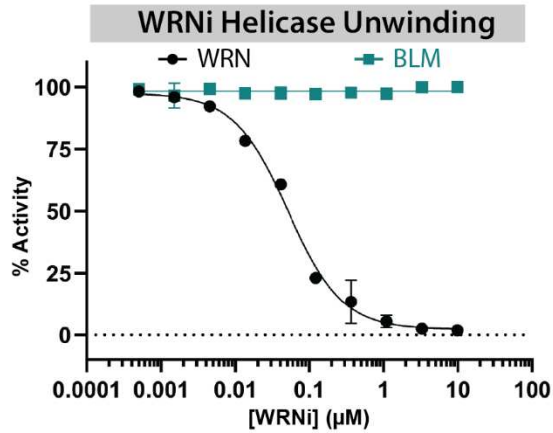
d



e



f



g

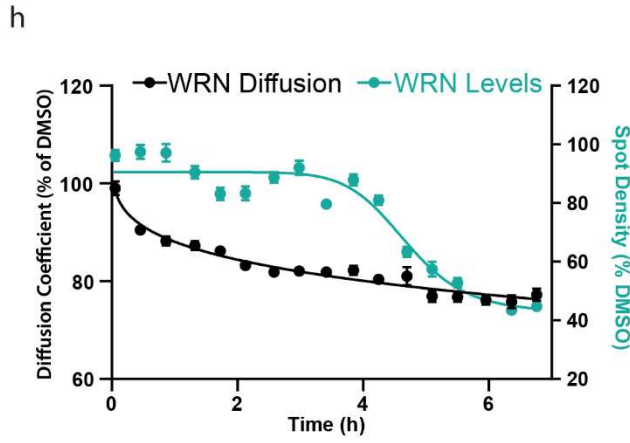
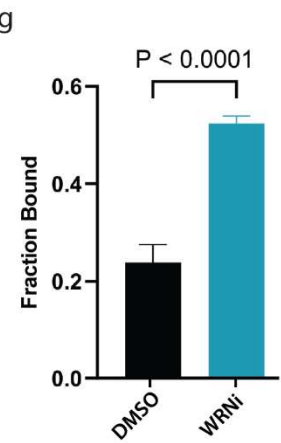
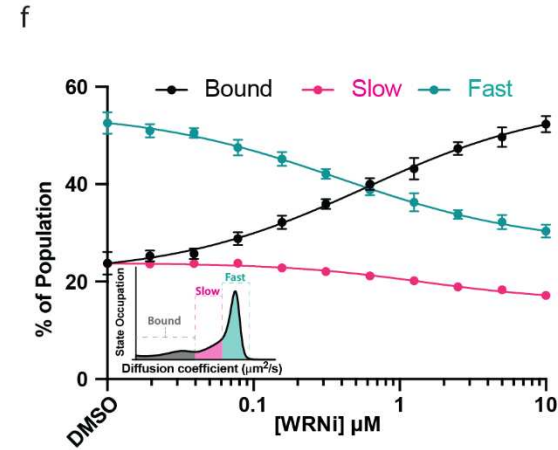
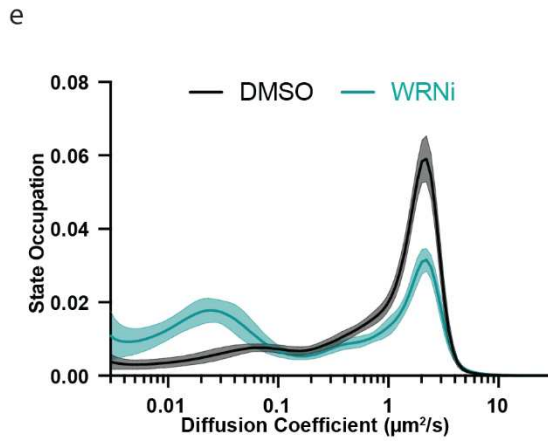
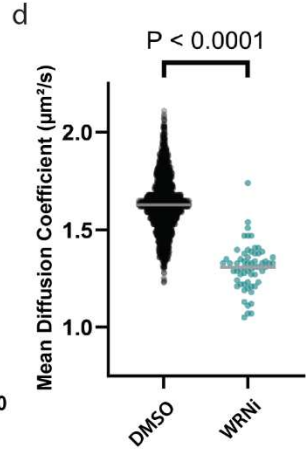
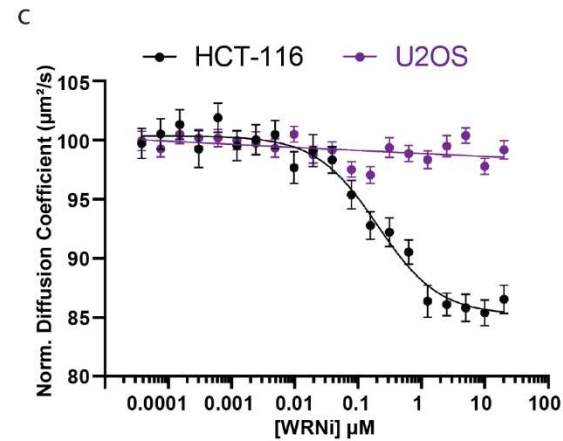
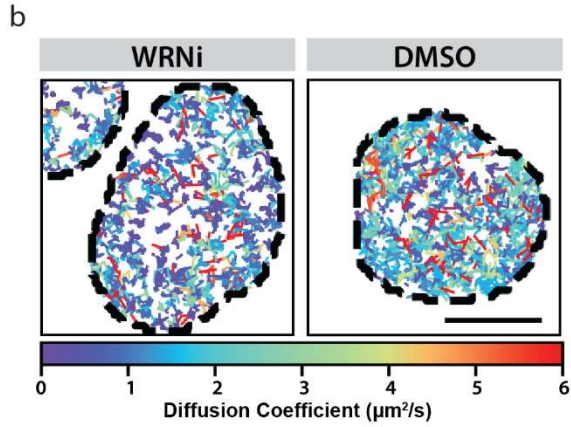
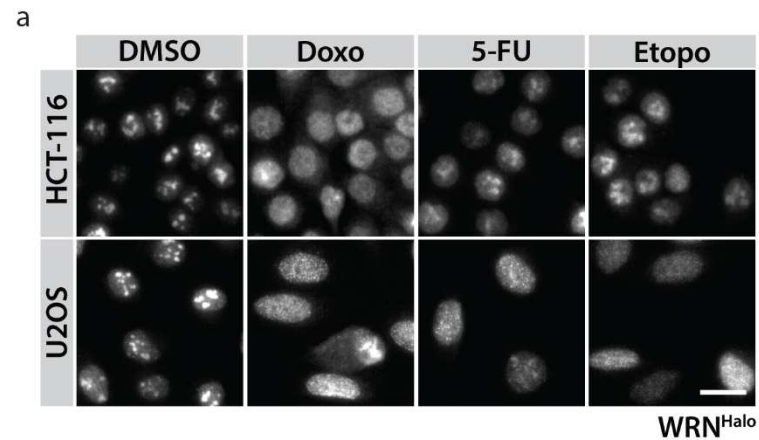
	Helicase		ATPase	
	WRN	BLM	WRN	BLM
IC ₅₀ (μM)	0.05	>10	0.06	>10

	γH2A.X		Viability	
	HCT-116	HT-29	HCT-116	HT-29
EC ₅₀ (μM)	0.10	>10	0.05	>10

664 **Fig. 1: HRO761 is a specific and potent WRN inhibitor.**

665 **a.** Chemical structure of HRO761 (WRNi). **b.** WRN inhibition leads to induction of the DNA damage
666 response in MSI-H cells. Phospho-histone H2A.X (Ser139) (γ H2A.X) staining was used to visualize DNA
667 damage in MSI-H (HCT-116, SW-48) and MSS (HT-29, U2OS) cells after 24 h treatment with indicated
668 compounds. Scale bar = 20 μ m. **c.** Quantification of γ H2A.X signal levels in cells in **b**, normalized to DMSO
669 and Etoposide. Graphs represent averages of at least 3 plate replicates, consisting of at least 6 fields of
670 view (FOVs). **d.** WRN inhibition by WRNi leads to an induction of the DNA damage response resulting in
671 apoptosis. HCT-116 cells treated with 10 μ M WRNi and analyzed via Western to assess DNA damage
672 response markers. **e.** Dose response curves measuring viability of HCT-116 cells or HT-29 cells after
673 treatment with WRNi for 4 days. Graphs represent averages from n = 6 plates. **f.** Dose response curves
674 measuring *in vitro* WRN or BLM unwinding activity after treatment with WRNi. Graphs represent averages
675 from n = 4 replicates. WRN unwinding activity is normalized to DMSO and ATP- γ -S; BLM activity is
676 normalized to DMSO and 10 μ M BLMi. **g.** Summary of IC₅₀ or EC₅₀ values of WRNi in the indicated
677 biochemical and cellular assays. All curve fits were done by fitting a 4-parameter logarithmic regression
678 curve. All error bars represent standard deviation (s.d.). DMSO is dimethyl sulfoxide; BLMi is BLM inhibitor
679 Compound 2; Etopo is etoposide. MW is molecular weight.

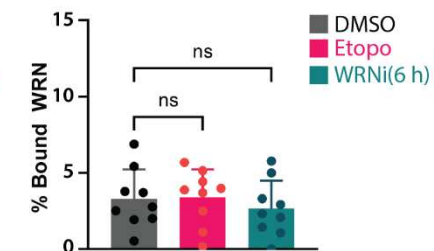
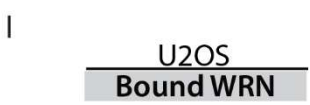
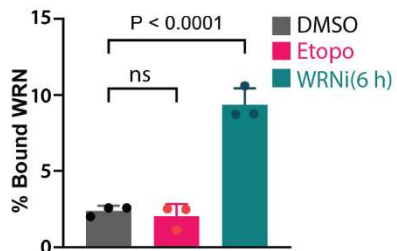
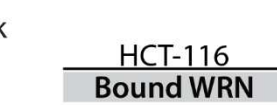
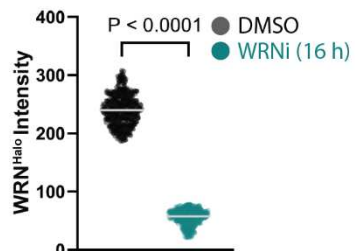
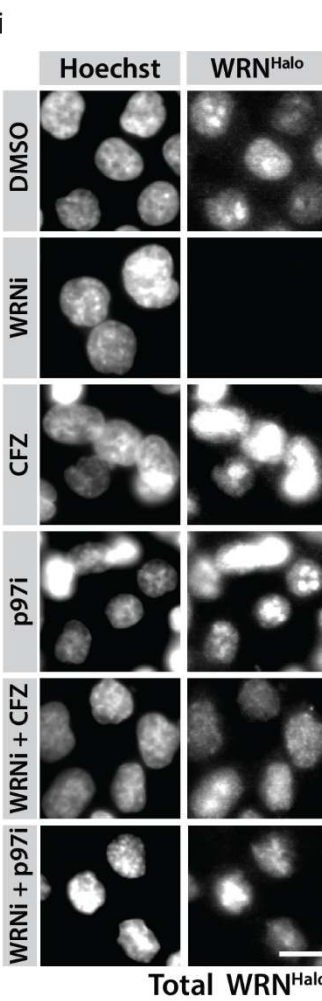
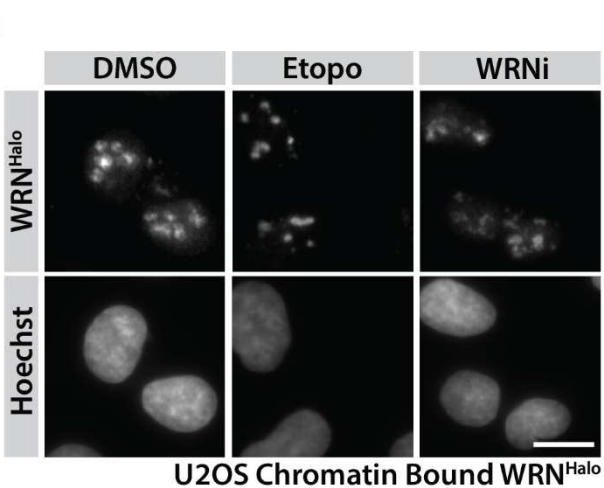
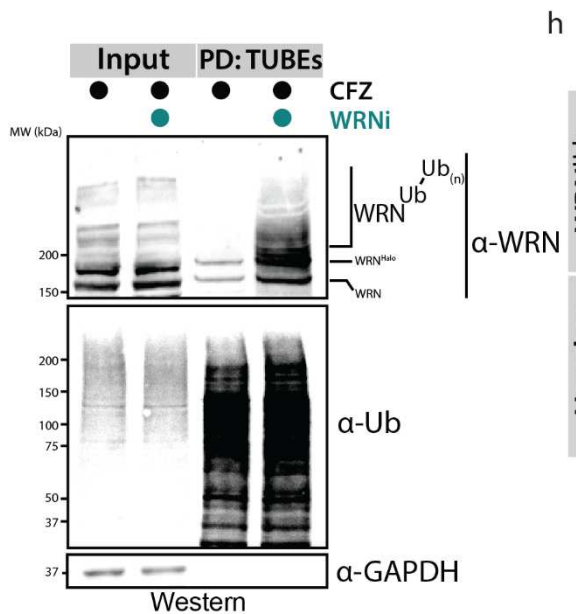
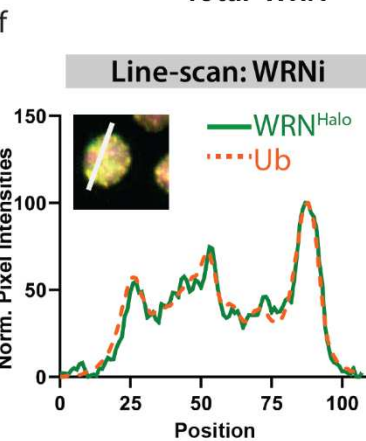
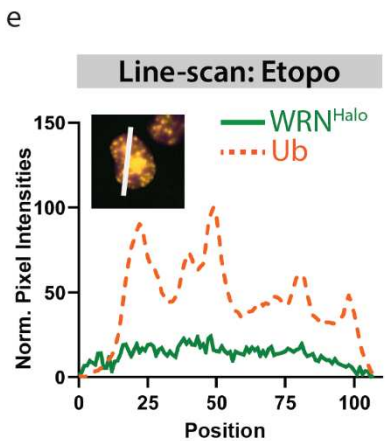
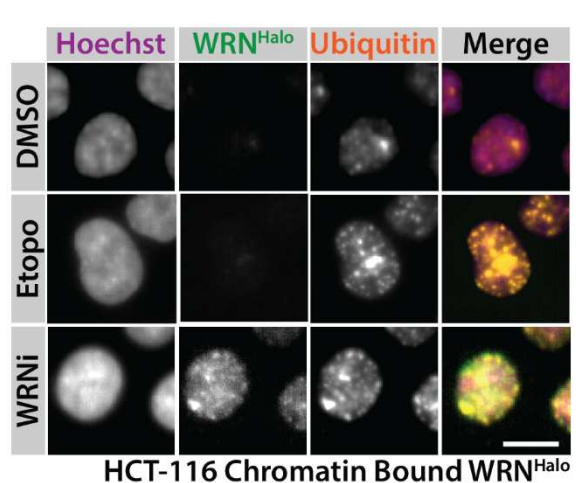
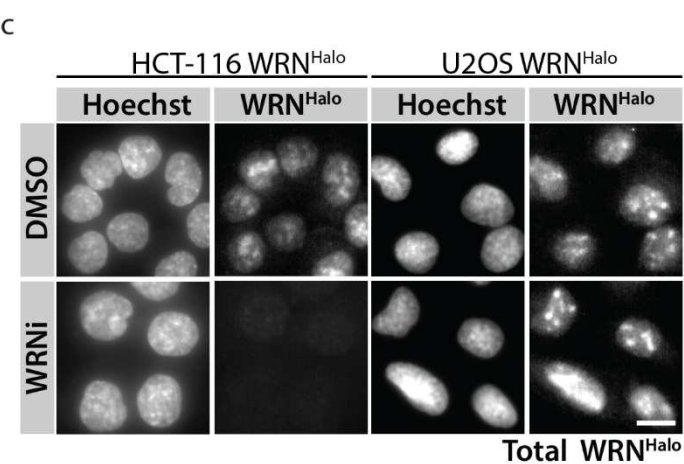
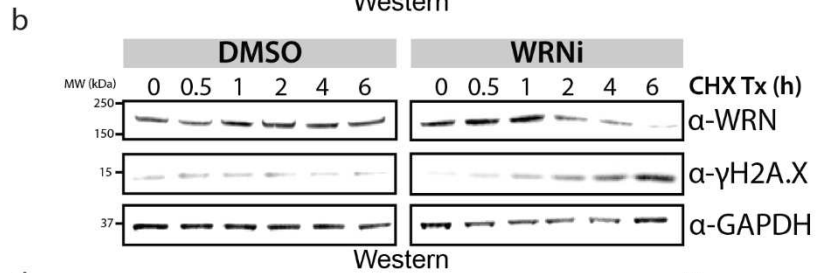
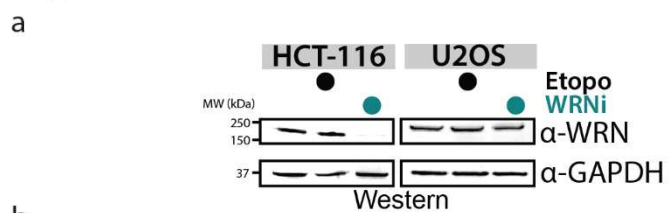
Figure 2



681 **Fig. 2: Single molecule tracking shows a change in WRN cellular dynamics in an MSI-H**
682 **dependent manner.**

683 **a.** WRN^{HALO} cell lines, HCT-116 and U2OS, were validated by visualizing the subcellular localization of WRN
684 in the presence or absence of DNA damaging compounds. WRN^{HALO} successfully translocates across
685 compartments, suggesting a functional protein. Scale bar = 20 μ m. **b.** The decrease in WRN diffusion
686 coefficient upon inhibition can be captured by SMT, showing a dramatic slowdown of WRN protein. WRN
687 inhibition leads to a decrease in molecule diffusion coefficient. Representative SMT track overlays over
688 Hoechst nuclear stain outlines, in the presence or absence of 10 μ M WRNi. Tracks are colored according
689 to the diffusion coefficient of the molecules. **c.** Inhibition of WRN only affects its mean diffusion coefficient
690 in MSI-H cells. Dose response curves with WRNi measuring the diffusion coefficient of WRN^{HALO} after 4 h
691 treatments in HCT-116^{WRN-HALO} or U2OS^{WRN-HALO}. Graph represents the average from $n = 4$ plates per
692 condition. Error bars represent standard error of the mean (s.e.m.). All curve fits were done by fitting a 4-
693 parameter logarithmic regression curve. **d.** Dot plot quantification of WRN diffusion coefficient from SMT
694 movies after treatment with 10 μ M WRNi. Each point represents the average WRN diffusion coefficient
695 within all the nuclei in an FOV. $n = 20$ plates. Lines represent sample medians. **e.** WRNi shifts a large
696 fraction of molecules from the free-diffusing state (“fast”) to the chromatin-bound (“bound”) state.
697 Distribution of diffusive states in HCT-116^{WRN-Halo} cells showing the relative proportion of WRN molecules
698 as a function of diffusion coefficient occupation, in the presence and absence of 10 μ M WRNi. Shaded
699 area represents s.d. **f.** Treatment with WRNi shows a dose-dependent increase in the bound fraction of
700 WRN, suggesting binding of WRN onto chromatin. Dose response curves with WRNi measuring the
701 different diffusive states of WRN protein. Inset is representation of how diffusive states are classified.
702 Error bars represent s.d.. **g.** Quantification from **f** of the chromatin bound fraction of WRN^{HALO} protein in
703 the presence or absence of 10 μ M WRNi. Error bars represent s.d.. **h.** SMT can capture changes in protein
704 diffusion before degradation is observed. Overlay of WRN^{HALO} diffusion coefficient and molecule spot
705 densities after treatment with 10 μ M WRNi over the indicated time points. Values are normalized to
706 DMSO by dividing all FOV-level measurements at each time point by the median DMSO value at that time
707 point, then multiplying by 100. $n = 2$ plates. Error bars represent s.e.m.. Curve fits were done by fitting a
708 4-parameter logarithmic regression curve. P-values were calculated using a two-tailed, unpaired t-test.
709 DMSO is dimethyl sulfoxide; WRNi is HRO761; 5-FU is 5-fluorouracil, Doxo is doxorubicin.

Figure 3

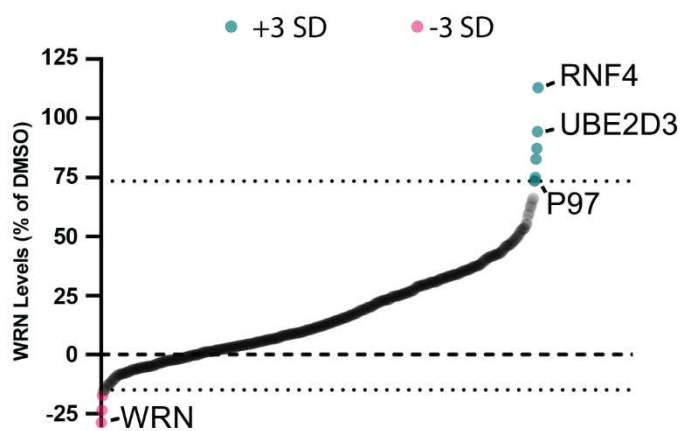


711 **Fig. 3: WRN Inhibition leads to its chromatin associated degradation.**

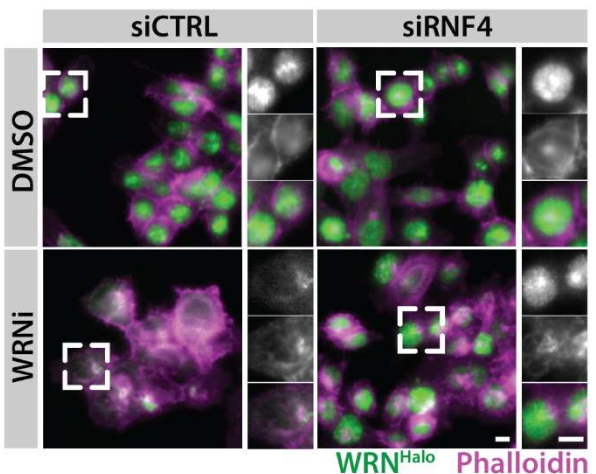
712 **a.** Inhibition of WRN leads to its degradation in an MSI-H dependent manner. HCT-116^{WRN-Halo} or U2OS^{WRN-}
713 ^{Halo} were treated with 10 μ M WRNi or etoposide for 16 h and analyzed by Western blot. **b.** Inhibition of
714 WRN in MSI-H leads to a change in the half-life of WRN protein. HCT-116^{WRN-Halo} were treated with 100
715 μ g/mL of cycloheximide (CHX) to inhibit protein synthesis in the presence or absence of 10 μ M WRNi,
716 then harvested at the indicated time points for Western blot analysis. Quantifications of CHX chase are in
717 **Extended Data Fig. 3d.** **c.** Loss of WRN protein after treatment with WRNi can be visualized by microscopy.
718 HCT-116^{WRN-Halo} or U2OS^{WRN-Halo} were treated with 10 μ M WRNi for 16 h then imaged to visualize total WRN
719 protein levels. Scale bar = 10 μ m. **d.** WRN inhibition leads to WRN trapping on chromatin and its
720 ubiquitylation. HCT-116^{WRN-Halo} cells were treated with 10 μ M WRNi or etoposide for 6 h, at which point
721 cells were permeabilized by treating with a mild detergent, then fixed and imaged. WRN signal retention
722 is only seen when WRN is inhibited, and not with general DNA damaging compounds. Ubiquitin signal was
723 also observed to colocalize with WRN^{Halo} when probing with a ubiquitin antibody. Scale bar = 10 μ m. **e.**
724 Line-scan quantification of etoposide treated cells from **d**, showing a lack of co-localization of the ubiquitin
725 signal channel and the WRN signal channel. **f.** Line-scan quantification of WRNi treated cells from **d**,
726 showing clear colocalization of the ubiquitin and WRN signal channels. **g.** WRN inhibition leads to its
727 ubiquitylation. Tandem ubiquitin binding entities (TUBEs) pulldown (PD) of HCT-116 cells after treatment
728 with 10 μ M WRNi for 6 h in the presence of 1 μ M carfilzomib (CFZ). Blotting for endogenous WRN using
729 an α -WRN antibody shows higher molecular weight species in the TUBEs pull down only in the presence
730 of WRNi. **h.** WRN chromatin trapping upon its inhibition is MSI-H dependent. Cells were treated with WRNi
731 as in **d** but using the MSS cell line U2OS^{WRN-Halo}. **i.** Degradation of WRN is dependent on the p97/VCP-
732 proteasome axis. HCT-116^{WRN-Halo} were treated with 10 μ M of WRNi and 1 μ M of either CB-5083 (p97i) or
733 CFZ for 6 h, then imaged. WRN protein degradation by WRNi is rescued upon co-treatment with CFZ or
734 p97i. Quantifications are in **Extended Data Fig. 3f.** **j-l.** Quantifications of **c**, **d**, and **h**. Graph in **j** represents
735 averages from $n = 3$ plates, with each individual point representing one well. Graph in **k** represents
736 averages from $n = 3$ plates, each individual point is the average of 6 wells. Graph in **l** represents averages
737 from $n = 9$ plates, each individual point is the average of 6 wells. Error bars represent s.d.. DMSO is
738 dimethyl sulfoxide; WRNi is HRO761; CHX is cycloheximide; CFZ is carfilzomib; Etopo is etoposide. P-values
739 were calculated using a two-tailed, unpaired Student's t-test. ns = not significant. MW is molecular weight.

Figure 4

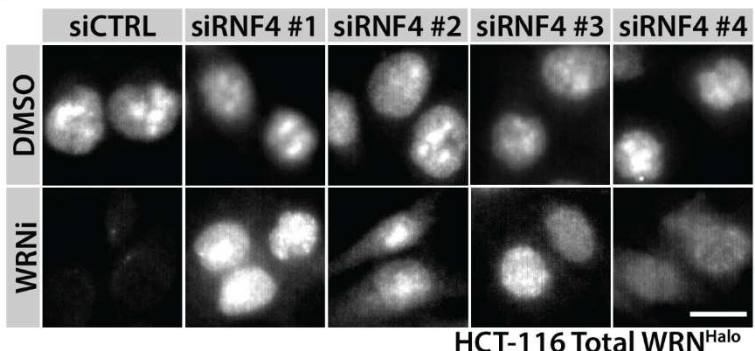
a



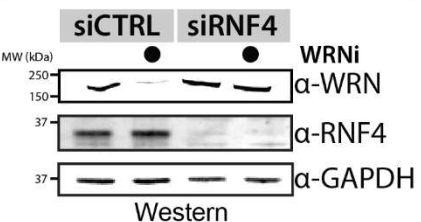
b



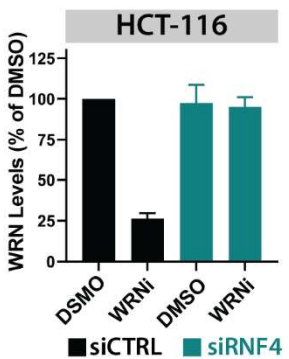
c



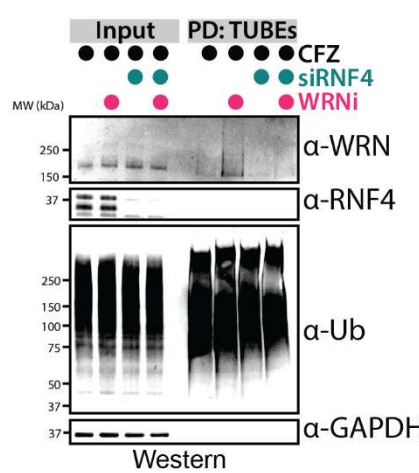
d



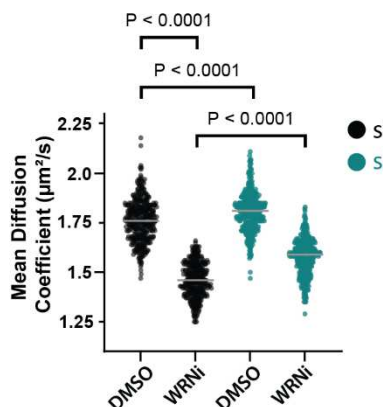
e



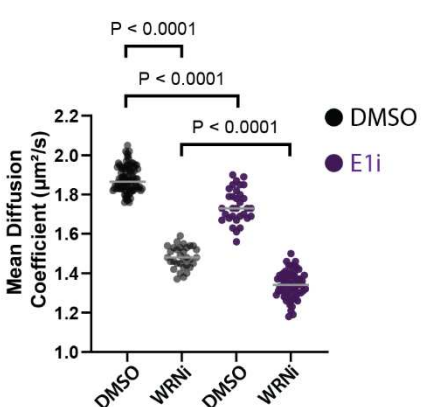
f



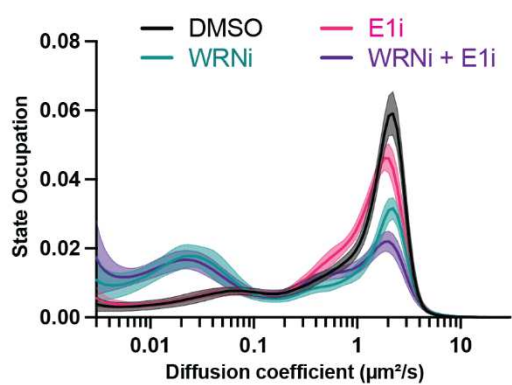
g



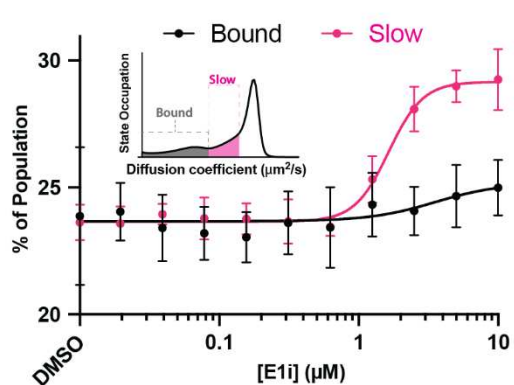
h



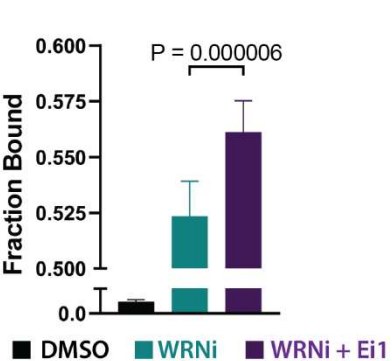
i



j



k

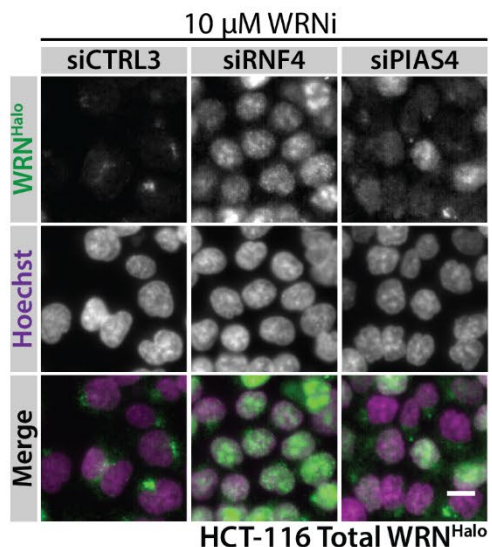


741 **Fig. 4: Phenotypic siRNA screen identified RNF4 as the ubiquitin E3 ligase targeting WRN for**
742 **degradation.**

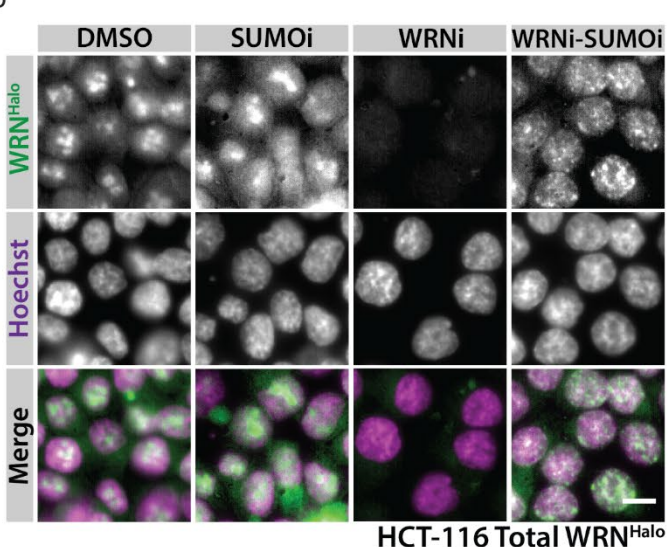
743 **a.** A phenotypic siRNA screen identified genes involved in the degradation of WRN after WRNi treatment.
744 Colored circles indicate hits that are 3 standard deviations (SD) from the mean. Quantification of WRN
745 protein levels after treatment with SMARTpool siRNAs in the presence or absence of 10 μ M WRNi for 24
746 h. Depletion of RNF4 leads to stabilization of WRN protein in the presence of WRNi. UBE2D3 is an E2
747 known to interact with RNF4. **b.** Representative images of HCT-116^{WRN-Halo} cells the siRNA screen
748 performed in **a**, showing a rescue of WRNi-induced degradation of WRN when RNF4 is depleted. Scale
749 bars = 10 μ m. **c.** Decomplexifying the siRNA SMARTpool validates RNF4 as the ligase responsible for WRN
750 degradation by WRNi treatment. Representative images of HCT-116^{WRN-Halo} cells show all individual RNF4
751 siRNA oligos rescue the degradation phenotype induced by WRNi. Scale bar = 10 μ m. Quantifications are
752 in **Extended Data Fig. 4c**. **d.** Western blot analysis validates RNF4 as the ligase responsible for degradation
753 of WRN induced by WRNi. HCT-116 cells were treated with siRNF4 oligos for 24 h, then treated with or
754 without 10 μ M WRNi for an additional 24 h, at which point cells were lysed and analyzed by Western blot
755 with indicated antibodies. **e.** Quantifications of **d**. Graphs represent the mean value of $n = 2$ Western blot
756 runs. Error bars represent s.d.. **f.** Depletion of RNF4 directly prevents ubiquitylation of WRN after WRNi
757 treatment. HCT-116 cells were treated with siRNF4 oligos for 24 h, then cotreated with or without 10 μ M
758 of WRNi for 6 h. All samples were treated with CFZ to stabilize ubiquitin-modified proteins. TUBEs
759 pulldowns (PD) and Western blot analysis were performed, probing with indicated antibodies. High
760 molecular weight WRN species are detected in the TUBEs PD when treated with WRNi, which are not
761 observed when treated with siRNF4 oligos, suggesting ubiquitylation of WRN is dependent on RNF4. **g.**
762 RNF4 depletion leads to a slight but significant increase in the mean diffusion coefficient of WRN. Dot
763 plots of WRN diffusion coefficient via SMT after co-treatment with siRNF4 and either DMSO or WRNi. Each
764 point represents the average WRN diffusion coefficient within all the nuclei in an FOV. $n = 4$ plates. Lines
765 represent sample medians. **h.** The ubiquitin pathway is involved in regulating WRN dynamics. Dot plots of
766 WRN diffusion coefficient via SMT after co-treatment with the ubiquitin-activating enzyme (E1) inhibitor
767 (E1i) and either DMSO or WRNi. E1i treatment caused a reduction in the diffusion coefficient of WRN. This
768 decrease in diffusion was exacerbated by cotreatment with WRNi. Each point represents the average WRN
769 diffusion coefficient within all the nuclei in an FOV. $n = 4$ plates. **i.** Distribution of diffusive states in HCT-
770 116^{WRN-Halo} cells showing the relative proportion of WRN molecules as a function of diffusion coefficient
771 occupation after treatment with 1 μ M E1i in the presence or absence of 10 μ M WRNi. E1 inhibition leads
772 to a shift from the “fast” to the “slow” state of WRN molecules. This shift is exacerbated by the
773 cotreatment with WRNi. Shaded area represents s.d.. **j.** Treatment with E1i shows a dose-dependent
774 increase in the slow fraction of WRN, suggesting that the ubiquitin pathway regulates WRN dynamics.
775 Dose response curves with E1i measuring the “bound” and “slow” fractions of WRN protein. Inset is
776 representation of how diffusive states are classified. Error bars represent s.d.. **k.** Bar graph quantification
777 of the fraction bound of WRN^{Halo} protein after WRNi treatment in the presence or absence of E1i. Error
778 bars represent s.d. DMSO is dimethyl sulfoxide; WRNi is HRO761; E1i is TAK-243; CFZ is carfilzomib. P-
779 values were calculated using a two-tailed, unpaired Student’s t-test. ns = not significant. MW is molecular
780 weight.

Figure 5

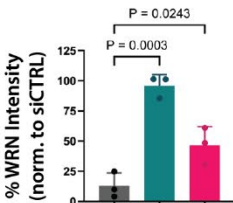
a



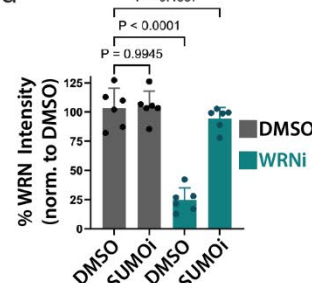
b



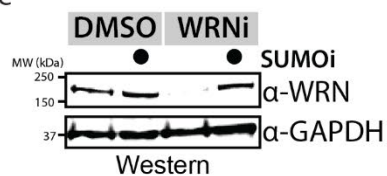
c



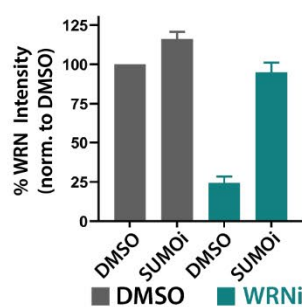
d



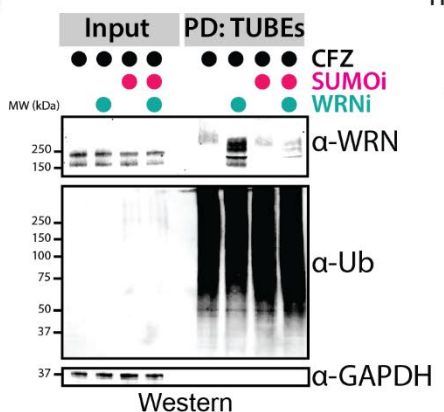
e



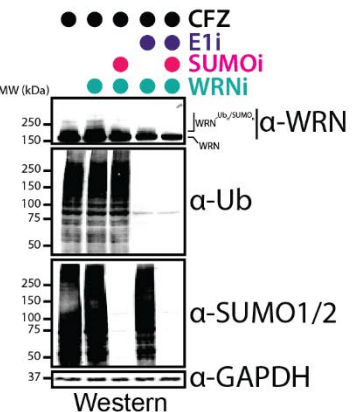
f



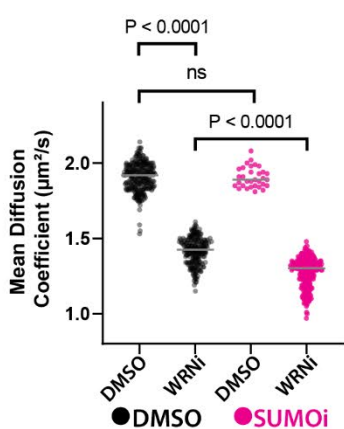
g



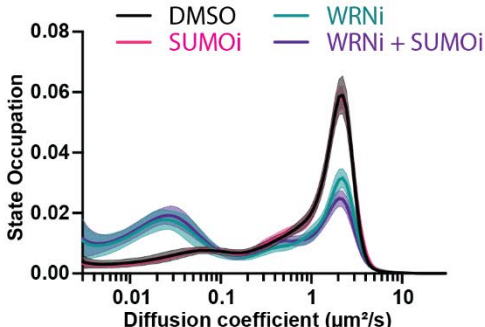
h



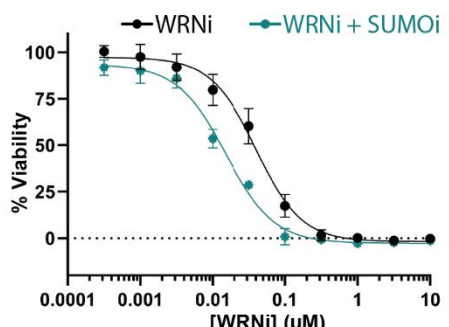
i



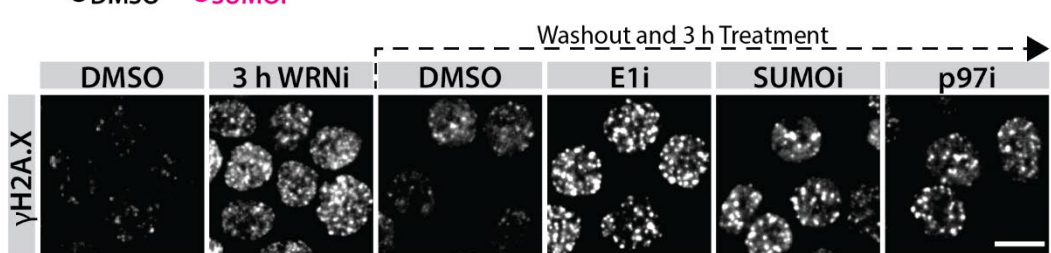
j



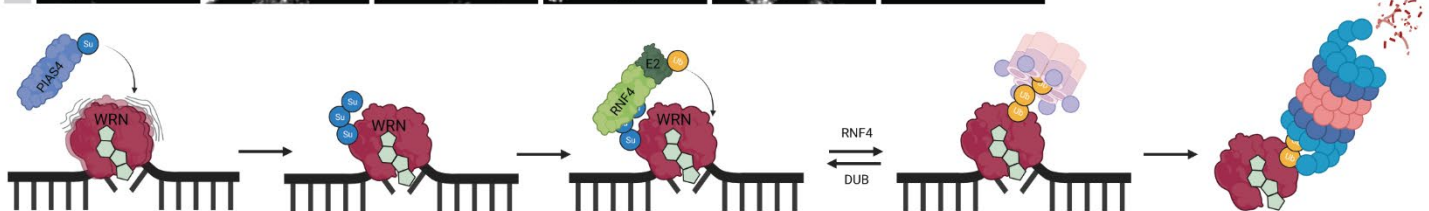
k



l



m



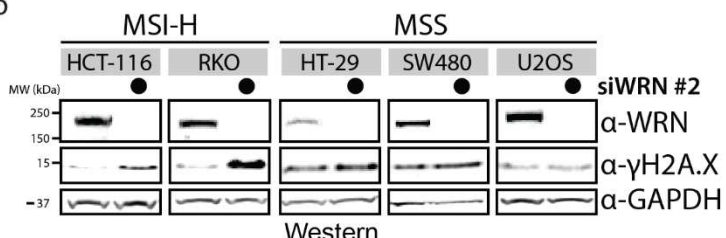
782 **Fig. 5: The PIAS4-RNF4 axis is responsible for the chromatin-associated degradation of WRN.**
783 **a.** WRN degradation is dependent on the SUMO E3 ligase PIAS4. HCT-116^{WRN-Halo} cells were treated with
784 the indicated siRNA oligos for 24 h, and subsequently treated with 10 μ M of WRNi for 24 h then imaged.
785 WRN degradation is rescued by the depletion of RNF4, and partially rescued by PIAS4 depletion. **b.**
786 SUMOylation is required for WRN degradation induced by WRNi. HCT-116^{WRN-Halo} cells were treated with
787 1 μ M of the SUMO-activating enzyme (SAE) inhibitor ML792 (SUMOi) in the presence or absence of 10
788 μ M WRNi, for 6 h and then fixed for imaging. Treatment with SUMOi results in a full rescue of the WRN
789 degradation phenotype. **c** and **d**. Quantifications of **a** and **b**, respectively. Graphs represent the average
790 of $n = 3$ plates for siRNA experiments and $n = 6$ plates for the small molecule experiments. Each dot
791 represents the average of 6 wells, and 6 FOVs per well. Error bars represent s.d.. **e.** Whole cell lysate
792 analysis shows SUMOylation is necessary for the degradation of WRN induced by WRNi. HCT-116 cells
793 were treated with 1 μ M SUMOi in the presence or absence 10 μ M WRNi 16 h, at which point cells were
794 lysed and analyzed by Western blot with indicated antibodies. Western blot analysis of cells showing WRN
795 protein levels are stabilized when treated with SUMOi. **f.** Quantification of **e**. Graphs represent the mean
796 value of $n = 2$ Western blot runs. Error bars represent s.d.. **g.** Inhibition of the SUMO pathway directly
797 prevents ubiquitylation of WRN after WRNi treatment. HCT-116 cells were treated with 1 μ M SUMOi in
798 the presence or absence of 10 μ M of WRNi for 6 h. All samples were treated with CFZ to stabilize ubiquitin-
799 modified proteins. TUBEs pulldowns (PD) and Western blot analysis were performed, probing with
800 indicated antibodies. High molecular weight WRN species are detected in the TUBEs PD when treated with
801 WRNi, which are not observed when treated with SUMOi, suggesting that the SUMO pathway is required
802 for the ubiquitylation of WRN upon its inhibition by WRNi. **h.** Whole cell lysate analysis by Western blot
803 showing that higher molecular weight WRN species are dependent on the SUMO and ubiquitin pathways.
804 Co-treatment with WRNi in the presence or absence of E1i and SUMOi show the disappearance of higher
805 molecular weight species when co-treated with SUMOi or E1i, and a full disappearance of these species
806 when co-treated with both SUMOi and E1i. **i.** Dot plots of WRN diffusion coefficient via SMT after co-
807 treatment with SUMOi and either DMSO or WRNi. Each point represents the average diffusion coefficient
808 of all the nuclei in an FOV. $n = 4$ plates. Lines represent sample medians; P-value was calculated using a
809 two-tailed, unpaired t-test. Co-treatment with both compounds leads to a further decrease in the
810 diffusion coefficient of WRN. **j.** Distribution of diffusive states for WRN^{HALO} in HCT-116^{WRN-Halo} after
811 treatment with 1 μ M of SUMOi in the presence or absence of 10 μ M WRNi, showing that SUMOi leads to
812 a decrease of the “fast” moving WRN molecules. **k.** Inhibition of the SUMO pathway synergizes with WRN
813 inhibition. Dose response of WRNi in HCT-116 cells treated in the absence or presence of 10 nM SUMOi
814 showing a shift in the EC₅₀ viability of WRNi. **l.** Failure to extract trapped WRN leads to persistent DNA
815 damage. Treating HCT-116 cells with WRNi for 3 h, then washing and replenishing with fresh growth media
816 containing 1 μ M of the indicated inhibitors show a retention in DNA damage as measured by γ H2A.X when
817 the SUMO-ubiquitin axis is perturbed. Scale bar = 10 μ m. **m.** Model for targeting trapped WRN to
818 proteasomal degradation by WRNi. WRN that is bound to chromatin surveying DNA damage in MSI-H cells
819 becomes trapped upon inhibition by WRNi. This stalled WRN is SUMOylated by the SUMO ligase PIAS4.
820 SUMOylated WRN recruits the STUbL RNF4, leading to its ubiquitylation. Ubiquitylated WRN is extracted
821 from chromatin by p97/VCP, leading to its degradation by the proteasome. DMSO is dimethyl sulfoxide;
822 WRNi is HRO761; E1i is TAK-243; SUMOi is ML-792; CFZ is carfilzomib. P-values were calculated using a
823 two-tailed, unpaired Student’s t-test. ns = not significant. MW is molecular weight.

Extended Data Figure 1

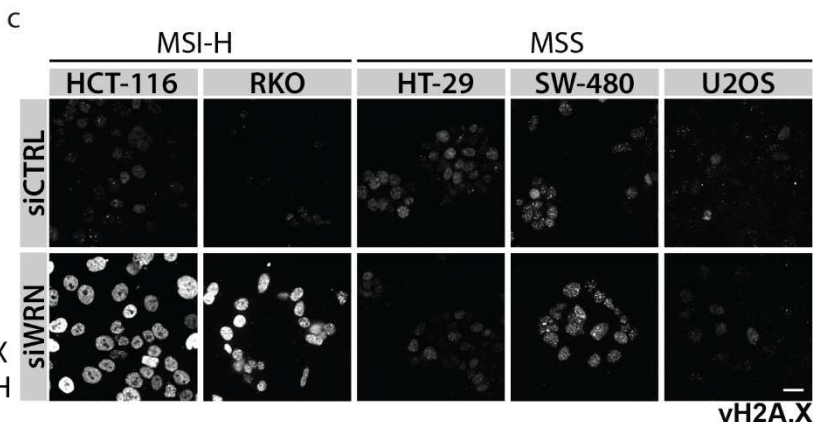
a



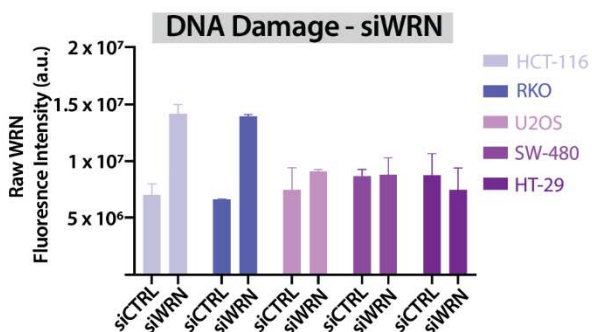
b



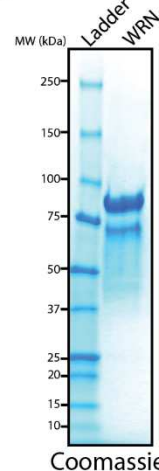
c



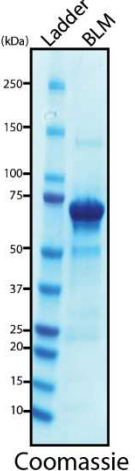
d



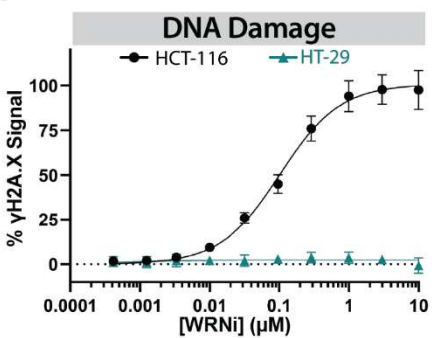
e



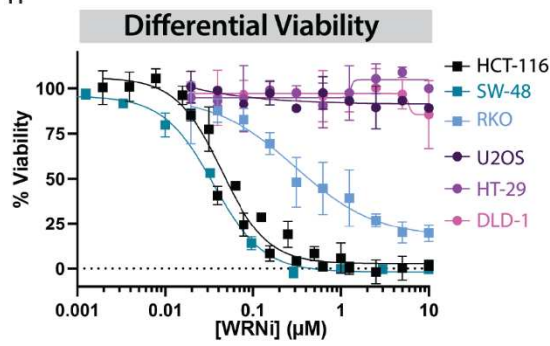
f



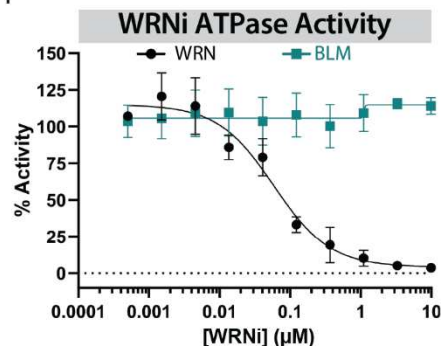
g



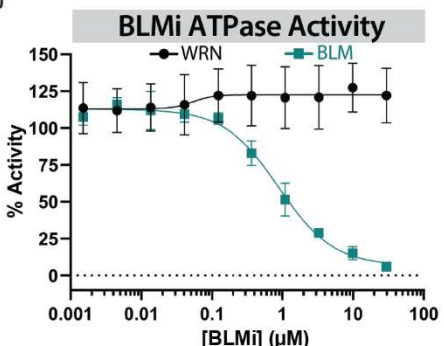
h



i



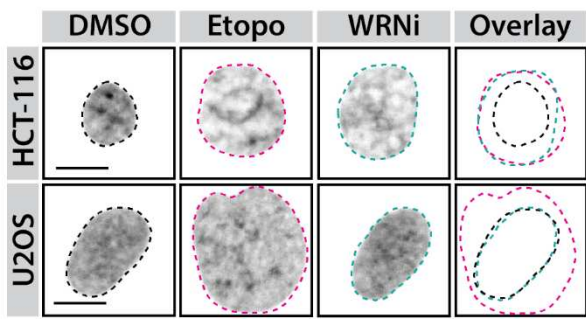
j



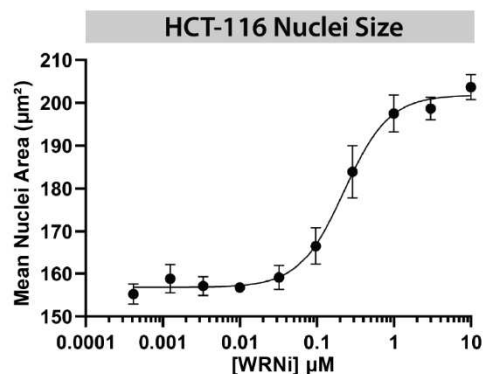
825 **Extended Data Fig. 1:**
826 **a.** Whole cell lysates of HCT-116 after siRNA depletions of WRN for 24 h and probing with a WRN antibody
827 show a robust loss of WRN protein. **b.** WRN depletion is synthetic lethal in MSI-H cells but not MSS cells.
828 Whole cell lysates in the indicated cell lines after treatment with siWRN or siCTRL oligos for 48 h, and
829 subsequently analyzed for DNA damage induction by Western blot. **c.** As in **b**, but cells were fixed in
830 paraformaldehyde after siRNA treatments, and DNA damage was measured by measuring γ H2A.X levels
831 via immunofluorescence. Scale bar = 20 μ m. **d.** Quantifications of **c**. Each graph represents the mean of n
832 = 3 plates. **e.** Purification of WRN protein from SF9 insect cells. Coomassie gel staining shows a product of
833 the expected protein molecular weight after purification. **f.** Protein purification of BLM protein from *E.*
834 *coli*. Coomassie gel staining shows a product of the expected protein molecular weight after purification.
835 **g.** DNA damage induction in MSI-H cells after WRN inhibition is dose-dependent. Dose response curves
836 measuring DNA damage response via γ H2A.X levels in HCT-116 cells or HT-29 cells after treatment with
837 WRNi for 24 h. Graphs represent averages from n = 6 plates. **h.** Cell viability panel of MSI-H and MSS cells
838 showing the differential viability effect of WRN inhibition towards MSI-H cells. Dose response curves
839 measuring the viability of the indicated cell lines after WRNi treatment for 4 days. HCT-116, SW-48, and
840 RKO are MSI-H cells; U2OS, HT-29, and DLD-1 are MSS cells. Graphs represent averages from n = 3 plates.
841 All error bars represent standard deviation (s.d.). **i.** Dose response curves measuring the *in vitro* ATPase
842 activity of WRN or BLM after WRNi treatment. Graphs represent averages from n = 6 plates. All curve fits
843 were done by fitting a 4-parameter logarithmic regression curve. **j.** Purified BLM protein is active.
844 Benchmarking of BLM protein by treatment with BLMi. Dose responses measuring ATPase and helicase
845 inhibition by BLMi. All curve fits were done by fitting a 4-parameter logarithmic regression curve. All error
846 bars represent standard deviation (s.d.). DMSO is dimethyl sulfoxide; WRNi is HRO761; BLMi is the BLM
847 inhibitor Compound 2. MW is molecular weight.

Extended Data Figure 2

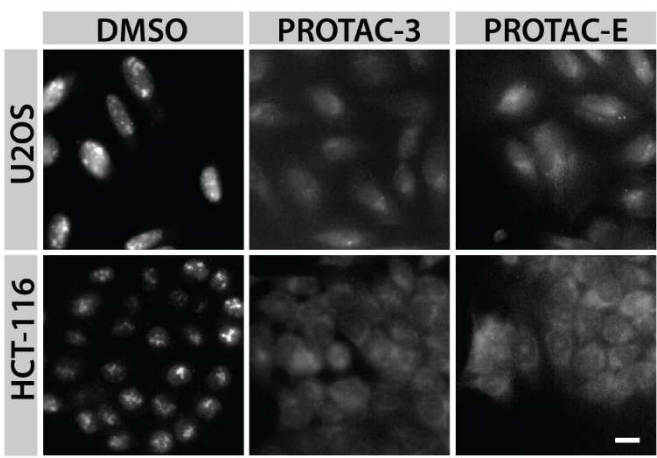
a



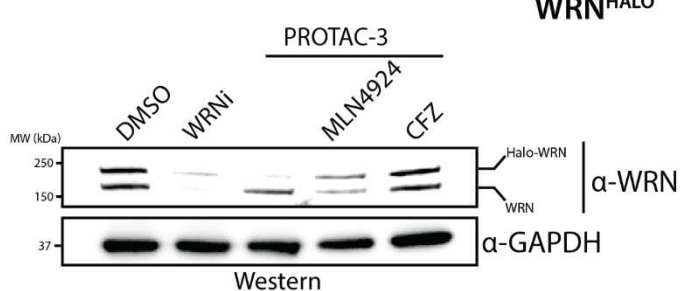
b



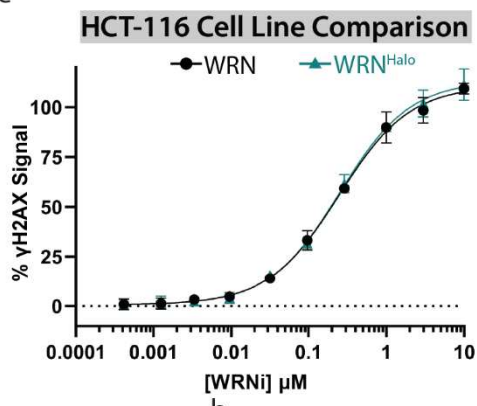
c



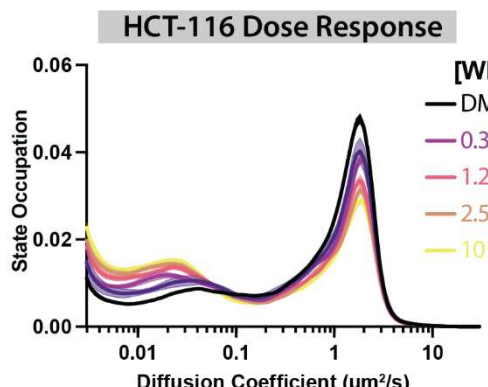
d



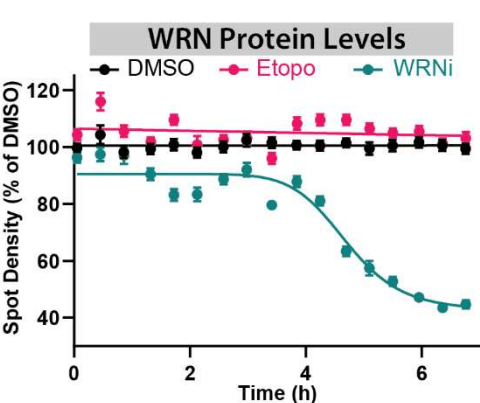
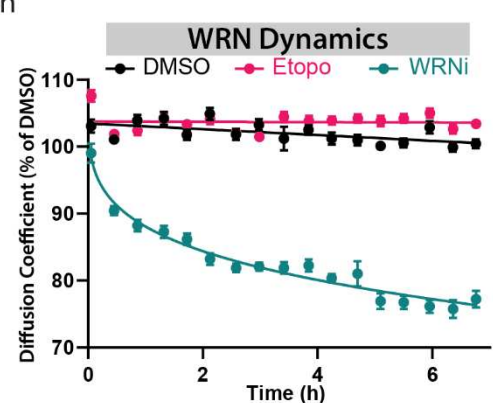
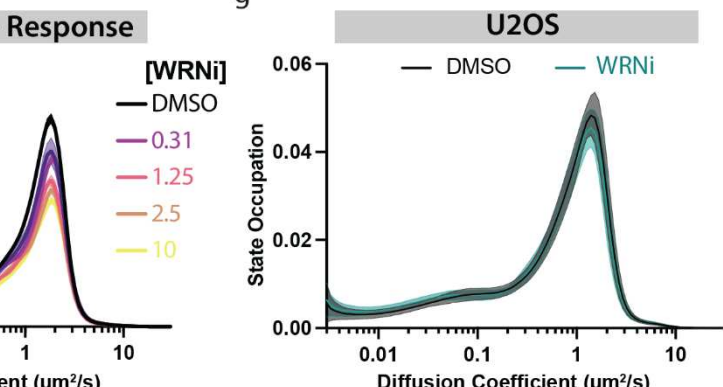
e



f



g



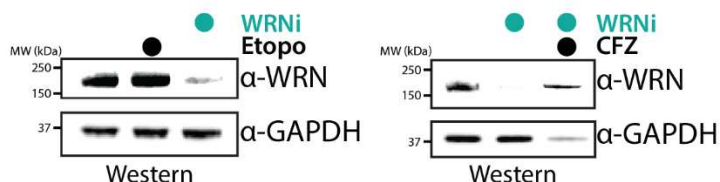
849 **Extended Data Fig. 2:**

850 **a.** WRNi causes morphological changes to nuclei due to DNA damage accumulation in MSI-H cells. Images
851 of Hoechst-stained nuclei of HCT-116 or U2OS cells treated in the presence or absence of 10 μ M WRNi or
852 etoposide for 24 h. Nuclei outlines are overlaid on top of each other, showing the large change in area
853 after WRNi treatment in HCT-116 cells. This increase in nuclei size is observed in HCT-116 and U2OS cells
854 after etoposide treatment. Scale bar = 10 μ m. **b.** Nuclear morphology changes induced by DNA damage
855 are dose-dependent. Dose response curve measuring nuclei area in HCT-116 cells after treatment with
856 WRNi for 24 h. Error bars represent s.d.. **c.** Validation of endogenous WRN Halo tagging of HCT-116 and
857 U2OS. WRN protein levels in HCT-116^{WRN-Halo} and U2OS^{WRN-Halo} visualized by staining with JF549 dye after
858 treatment with 10 μ M degraders of HaloTag, PROTAC-E or PROTAC-3, for 24 h. Scale bar = 10 μ m. **d.**
859 Treatment with Halo-PROTAC-3 leads to proteasomal dependent degradation of WRN^{Halo}. Further
860 validation of the WRN^{Halo} tag, showing Western blot analysis of HCT-116-WRN^{Halo} cells after treatment
861 with 10 μ M PROTAC-3 in the presence or absence of 2 nM CFZ or 5 nM MLN-4924 for 24 h. PROTAC-3
862 uses CUL2^{VHL} as a ligase, therefore CUL2 inhibition via MLN-4924 leads to a rescue of the WRN^{Halo}
863 degradation phenotype. **e.** Wild type HCT-116 cells and HCT-116-WRN^{Halo} cells have identical responses to
864 WRNi, suggesting WRN^{Halo} is functional. Dose response curves of HCT-116^{WT} and HCT-116-WRN^{Halo}
865 measuring DNA damage induction. Error bars represent s.d.. **f.** WRNi leads to a dose-dependent increase
866 of WRN molecules bound to chromatin. Distribution of diffusive states for WRN^{Halo} in increasing
867 concentrations of WRNi. WRNi leads to a decrease of free-disusing WRN molecules with a concomitant
868 increase in chromatin-bound WRN molecules. **g.** WRNi does not lead to chromatin trapping in MSS cells.
869 SMT measurements show that the distribution of WRN^{Halo} diffusive states in U2OS^{WRN-Halo} cells remains
870 unchanged in the presence or absence of 10 μ M WRNi. Shaded area represent s.d.. **h** and **i.** WRN diffusion
871 coefficient (**h**) and protein levels (**i**) remain unchanged upon DNA damage induction. Kinetic SMT of HCT-
872 116-WRN^{Halo} after treatment with 10 μ M WRNi or Etopo over the indicated time points. Error bars
873 represent s.e.m.. CFZ is carfilzomib; DMSO is dimethyl sulfoxide; WRNi is HRO761; Etopo is etoposide.
874 MW is molecular weight.

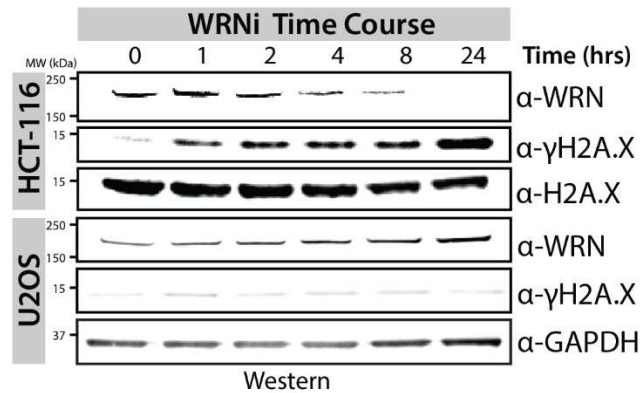
875

Extended Data Figure 3

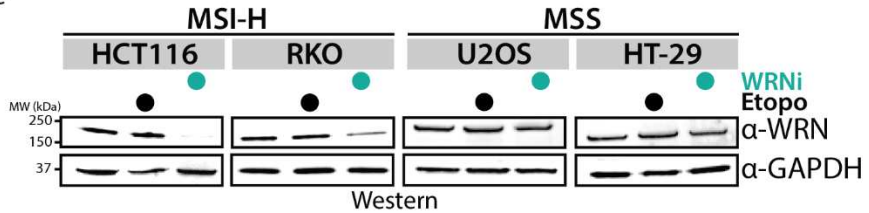
a



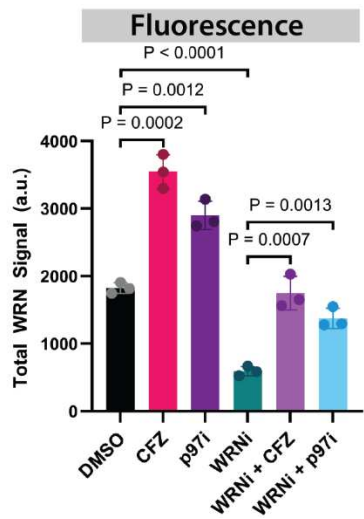
c



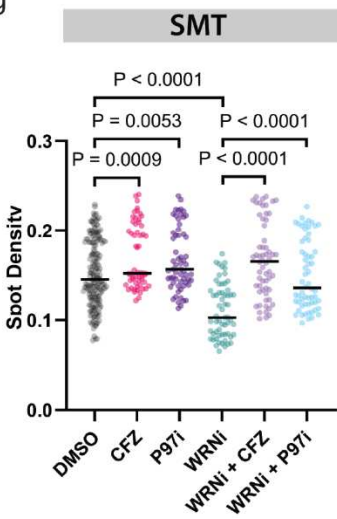
e



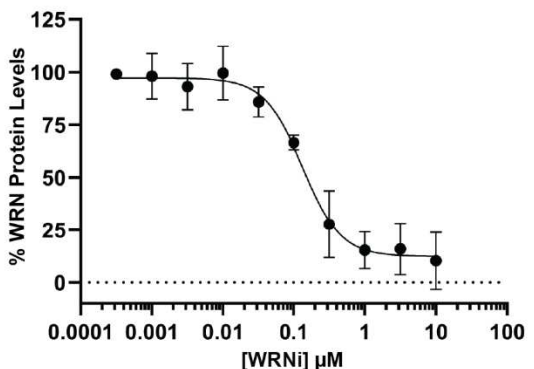
f



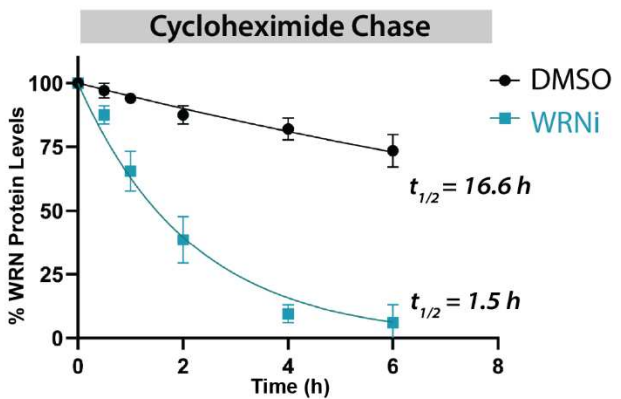
g



b



d

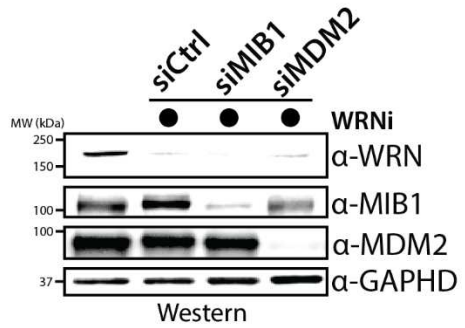


877 **Extended Data Fig. 3:**

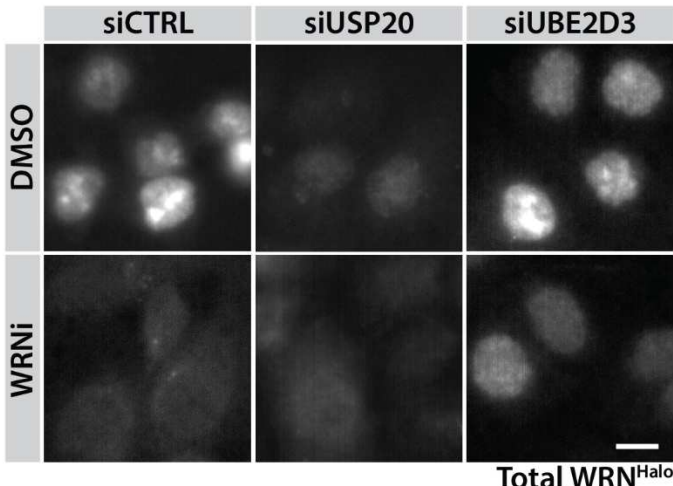
878 **a.** Degradation of WRN is induced by WRNi, but not by general DNA damage. Western blot analysis of
879 HCT-116 cells treated with 10 μ M etoposide or WRNi. This degradation is rescued by the addition of CFZ.
880 **b.** Dose response curves measuring WRN protein levels by staining HCT-116^{WRN-Halo} cells with JF549 after
881 treatment with WRNi for 24 h. Graphs represent averages from $n = 3$ plates, measuring 3 well per plate
882 and 6 FOVs per well. The curve fit was done by fitting a 4-parameter logarithmic regression curve. **c.**
883 Inhibition of WRN induces WRN degradation in a time-dependent manner in MSI-H cells. Steady state
884 Western blot analysis of HCT-116 or U2OS cells treated with 10 μ M WRNi over the indicated time points.
885 **d.** Quantification of **Fig. 3b.** WRN inhibition leads to a decrease in the half-life of WRN protein.
886 Cycloheximide (CHX) chase experiments in HCT-116 cells in the presence or absence of 10 μ M WRNi show
887 a dramatic decrease in the half-life of WRN protein upon its inhibition. Graphs represent $n = 2$ replicates.
888 The curve fit was done by fitting a half-life decay regression curve. **e.** WRN degradation upon its inhibition
889 is MSI-H dependent. The indicated MSI-H or MSS cell lines were treated as in **a** and analyzed by Western
890 blot with the indicated antibodies. **f.** Quantifications of **Fig. 3i.** Bar graphs are the mean of $n = 3$ replicates,
891 each point represents an the average of a well. Error bars represent s.d. **g.** SMT can be used to measure
892 protein degradation. SMT was used to measure WRN molecules after inhibition of the p97/VCP-
893 proteasome pathway, showing a rescue in protein degradation. Each point represents the average WRN
894 spot density within all the nuclei in an FOV. $n = 4$ plates. Lines represent sample medians. DMSO is
895 dimethyl sulfoxide; CFZ is carfilzomib; p97i is CB-5083; WRNi is HRO761. P-values were calculated using a
896 two-tailed, unpaired Student's t-test. MW is molecular weight.

Extended Data Figure 4

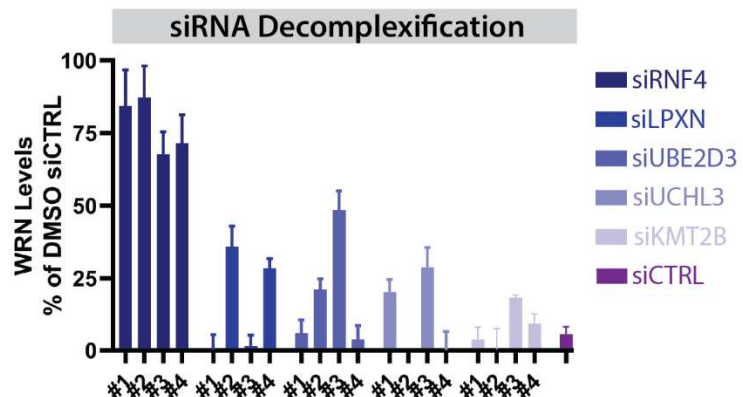
a



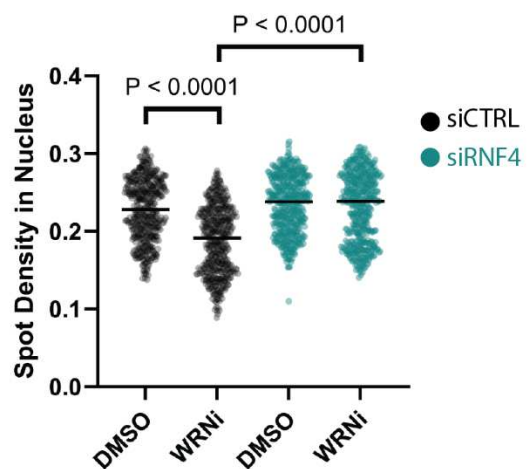
b



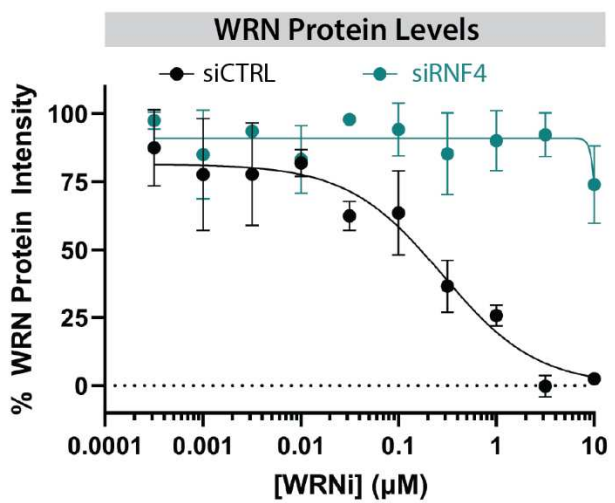
c



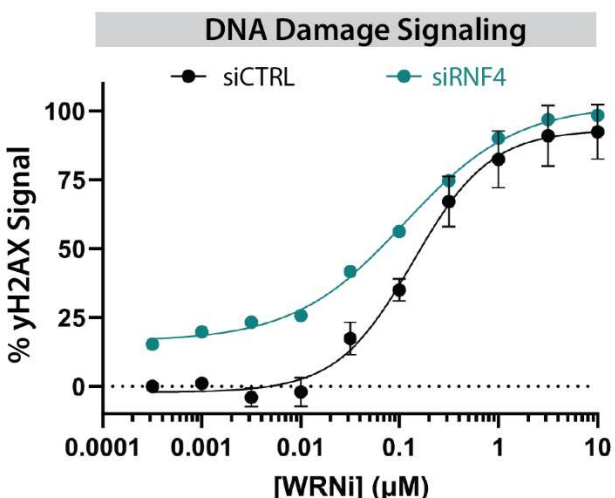
d



e



f

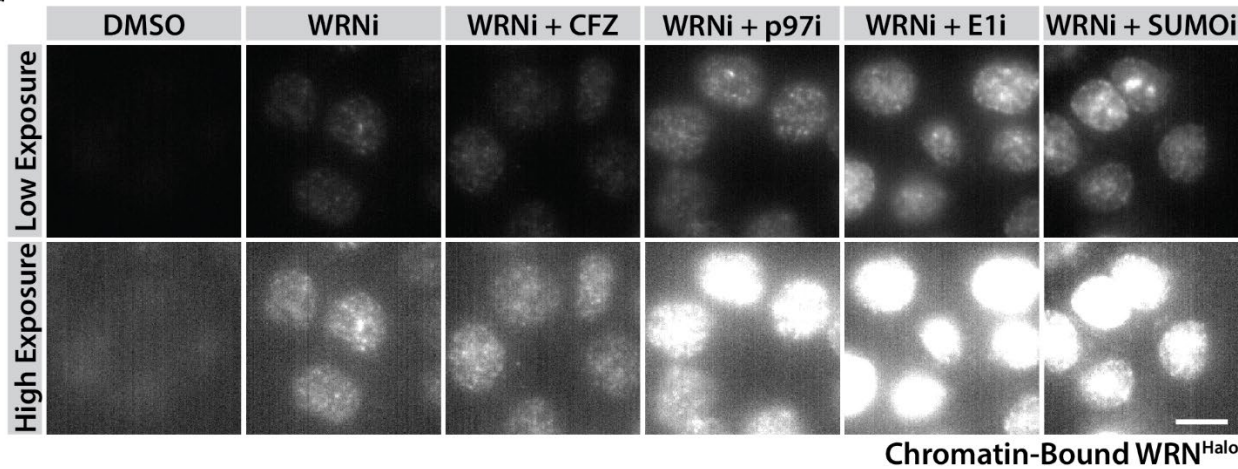


898 **Extended Data Fig. 4:**

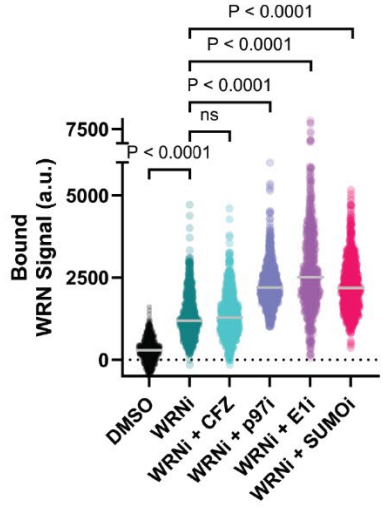
899 **a.** Previously reported E3 ligases of WRN are not responsible for the WRNi-dependent degradation
900 phenotype. HCT-116 were treated with indicated siRNA oligos for 24 h, and subsequently treated with 10
901 μ M WRNi for 16 h and analyzed by Western showing that depletion of the indicated E3 ligases does not
902 rescue the WRN degradation phenotype. **b.** Identification of additional ubiquitin pathway regulators of
903 WRN regulation. Representative images of HCT-116 cells after depletion of the indicated ubiquitin
904 pathway regulators. Scale bar = 10 μ m. **c.** Quantification of decomplexified siRNA screen hits from **Fig. 4a**
905 after treatment of HCT-116^{WRN-Halo} with indicated siRNA oligos for 24 h and then subsequent treatment
906 with 10 μ M WRNi for 24 h. Bar graphs are the average quantified WRN protein levels for each indicated
907 siRNA oligo of $n = 3$ plates. Error bars represent s.d.. **d.** SMT can be used to quantify protein degradation.
908 Depletion of RNF4 rescues WRN protein levels after WRN inhibition. WRNi dot plots showing the WRN
909 nuclear spot density from SMT experiments after co-treatment with siRNF4 and either DMSO or WRNi.
910 Each point represents the average WRN spot density within all the nuclei in an FOV. $n = 4$ plates. Lines
911 represent sample medians. **e.** RNF4 depletion rescues the WRN degradation phenotype. Dose response
912 curves measuring WRN protein levels by imaging HCT-116^{WRN-Halo} treated with the indicated siRNAs for 24
913 h, and subsequent treatment with WRNi for 24 h. Graphs represent averages from $n = 3$ plates, measuring
914 3 wells per plate and 6 FOVs per well. Error bars represent s.d.. **f.** Depletion of RNF4 exacerbates DNA
915 damage induced by WRNi. HCT-116 cells were depleted with indicated siRNAs for 24 h, and subsequently
916 subjected to a dose response of WRNi for 16 h. DNA damage was assessed by measuring γ H2A.X staining.
917 Graphs represent averages from $n = 3$ plates, measuring 3 wells per plate and 6 FOVs per well. Error bars
918 represent s.d.. All curve fits were done by fitting a 4-parameter logarithmic regression curve. DMSO is
919 dimethyl sulfoxide; WRNi is HRO761. P-values were calculated using a two-tailed, unpaired Student's t-
920 test. MW is molecular weight.

Extended Data Figure 5

a



b

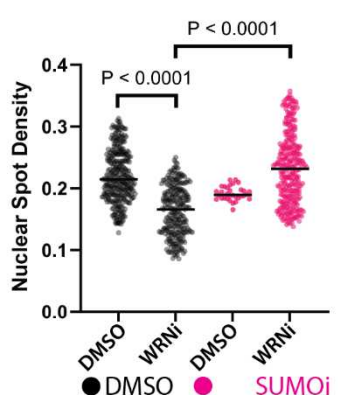


922 **Extended Data Fig. 5:**

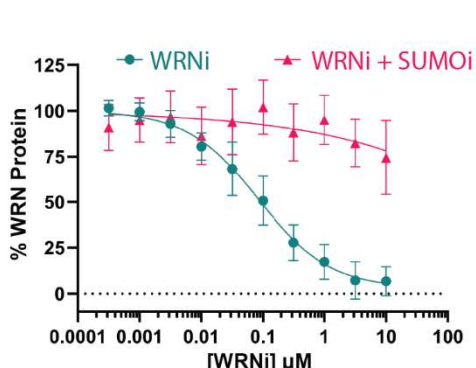
923 **a.** The SUMO-Ubiquitin-p97/VCP axis is required to remove trapped WRN from chromatin. Treatment of
924 HCT-116-WRN^{Halo} cells with 10 μ M WRNi in the presence or absence of 1 μ M of CFZ, p97i, E1i, or SUMOi,
925 followed by detergent extraction and imaging. **b.** Dot plot quantification of **a**. Each point represents an
926 individual cell, measuring the nuclear intensity of WRN. Bars represent the means of the populations.
927 DMSO is dimethyl sulfoxide, WRNi is HRO761; CFZ is carfilzomib; p97i is CB-5083; E1i is TAK-243; SUMOi
928 is ML-792. P-values were calculated using a two-tailed, unpaired Student's t-test. ns = not significant.

Extended Data Figure 6

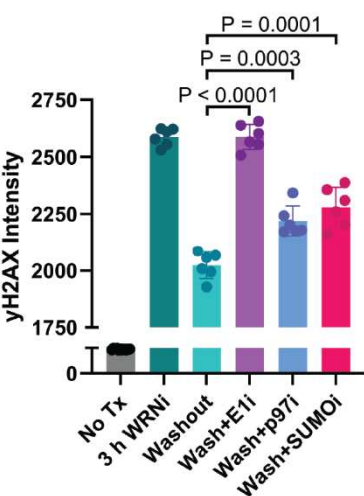
a



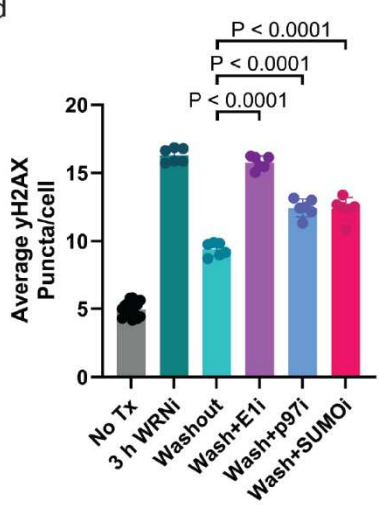
b



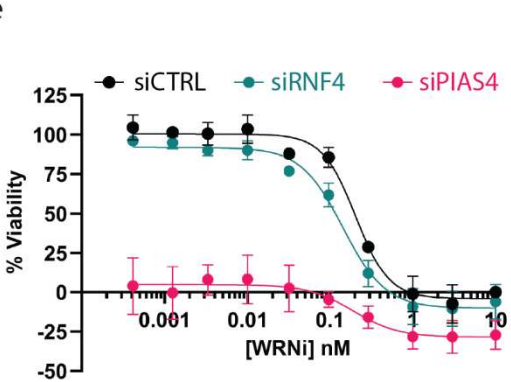
c



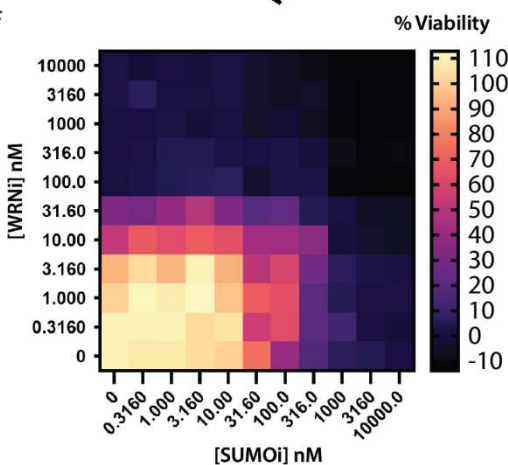
d



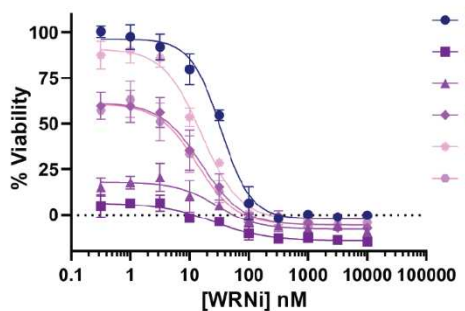
e



f

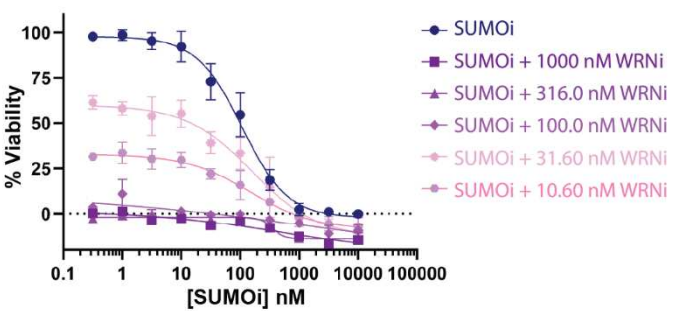


g



- WRNi
- WRNi + 1000 nM SUMOi
- WRNi + 316.0 nM SUMOi
- WRNi + 100.0 nM SUMOi
- WRNi + 31.60 nM SUMOi
- WRNi + 10.60 nM SUMOi

h



- SUMOi
- SUMOi + 1000 nM WRNi
- SUMOi + 316.0 nM WRNi
- SUMOi + 100.0 nM WRNi
- SUMOi + 31.60 nM WRNi
- SUMOi + 10.60 nM WRNi

930 **Extended Data Fig. 6:**

931 **a.** SMT can be used to elucidate molecular regulatory pathways, such as protein degradation. Inhibition
932 of SUMOylation rescues WRN protein levels after WRN inhibition. WRNi Dot plots showing the WRN
933 nuclear spot density from SMT experiments after co-treatment with SUMOi and either DMSO or WRNi.
934 Each point represents the average spot density within all the nuclei in an FOV. $n = 4$ plates. Lines represent
935 sample medians. **b.** Inhibition of SUMOylation prevents WRN degradation by WRNi. Dose response curves
936 measuring WRN protein levels by in HCT-116^{WRN-Halo} treated with WRNi in the presence or absence of 1
937 μM SUMOi, and subsequent treatment with WRNi for 24 h. Graphs represent averages from $n = 3$ plates,
938 measuring 3 well per plate and 6 FOVs per well. Error bars represent s.d. **c** and **d**. Quantification of
939 washout experiment in **Fig. 5l**. **d** quantifies the average $\gamma\text{H2A.X}$ nuclear intensities of an FOV, and **c**
940 quantifies the average number of $\gamma\text{H2A.X}$ puncta per nuclei in an FOV. Bar graphs in both **c** and **d** represent
941 the average of $n = 3$ plates. Each data point represents the average of one well, containing 6 FOVs. Error
942 bars represent s.d.. **e.** WRNi compound efficacy is independent of WRN degradation but shows potential
943 sensitization to inhibition of the PIAS4-RNF4 axis. HCT-116 cells were treated with the indicated siRNAs
944 for 24 h, followed by WRNi treatment at the indicated doses for 48 h. Cell viability was measured using a
945 CTG2 kit. Graphs represent averages from $n = 3$ plates. Error bars represent s.d. **f.** Co-treatment of WRNi
946 with SUMOi has potential synergy. Dose response matrix of both WRNi and SUMOi with indicated
947 concentrations of compound. HCT-116 cells were treated with indicated dose combinations for 48 h.
948 Viability was measured via CTG2. **g** and **h**. Quantifications of **f**, showing dose response plots for the
949 indicated concentration combinations. Graphs represent averages from $n = 3$ plates. Error bars represent
950 s.d.. All curve fits were done by fitting a 4-parameter logarithmic regression curve. DMSO is dimethyl
951 sulfoxide; WRNi is HRO761; E1 is TAK-243; SUMOi is ML-792; p97i is CB-5083. P-values were calculated
952 using a two-tailed, unpaired Student's t-test.